



HAL
open science

A systematic study of the escape of LyC and Ly α photons from star-forming, magnetized turbulent clouds

Taysun Kimm, Rebekka Bieri, Sam Geen, Joakim A Rosdahl, Jérémy Blaizot,
Léo Michel-Dansac, Thibault Garel

► To cite this version:

Taysun Kimm, Rebekka Bieri, Sam Geen, Joakim A Rosdahl, Jérémy Blaizot, et al.. A systematic study of the escape of LyC and Ly α photons from star-forming, magnetized turbulent clouds. 2021. hal-03817568v1

HAL Id: hal-03817568

<https://cnrs.hal.science/hal-03817568v1>

Preprint submitted on 23 Nov 2021 (v1), last revised 17 Oct 2022 (v2)

HAL is a multi-disciplinary open access archive for the deposit and dissemination of scientific research documents, whether they are published or not. The documents may come from teaching and research institutions in France or abroad, or from public or private research centers.

L'archive ouverte pluridisciplinaire **HAL**, est destinée au dépôt et à la diffusion de documents scientifiques de niveau recherche, publiés ou non, émanant des établissements d'enseignement et de recherche français ou étrangers, des laboratoires publics ou privés.

A systematic study of the escape of LyC and Ly α photons from star-forming, magnetized turbulent clouds

TAYSUN KIMM ¹, REBEKKA BIERI ², SAM GEEN ³, JOAKIM ROSDAHL ⁴, JÉRÉMY BLAIZOT ⁴,
LÉO MICHEL-DANSAC⁴ AND THIBAUT GAREL ⁵

¹*Department of Astronomy, Yonsei University, 50 Yonsei-ro, Seodaemun-gu, Seoul 03722, Republic of Korea*

²*Max Planck Institute for Astrophysics, Karl-Schwarzschild-Straße 1, 85748, Garching, Germany*

³*Anton Pannekoek Institute for Astronomy, Universiteit van Amsterdam, Science Park 904, NL-1098 XH Amsterdam, the Netherlands*

⁴*Univ Lyon, Univ Lyon1, Ens de Lyon, CNRS, Centre de Recherche Astrophysique de Lyon UMR5574, F-69230 Saint-Genis-Laval, France*

⁵*Observatoire de Genève, Université de Genève, 51 Ch. des Maillettes, 1290 Versoix, Switzerland*

(Received October 8, 2021)

ABSTRACT

Understanding the escape of Lyman continuum (LyC) and Lyman α (Ly α) photons from giant molecular clouds (GMCs) is crucial if we are to study the reionization of the Universe and to interpret spectra of observed galaxies at high redshift. To this end, we perform high-resolution, radiation-magneto-hydrodynamic simulations of GMCs with self-consistent star formation and stellar feedback. We find that a significant fraction (15–70%) of ionizing radiation escapes from the simulated GMCs with different masses (10^5 and $10^6 M_{\odot}$), as the clouds are dispersed within about 2–5 Myr from the onset of star formation. The fraction of LyC and Ly α photons leaked is larger when the GMCs are less massive, metal-poor, more turbulent, and less dense. The most efficient leakage of LyC radiation occurs when the total star formation efficiency of a GMC is about 20%. The escape of Ly α shows a trend similar to that of LyC photons, except that the fraction of Ly α photons escaping from the GMCs is larger ($f_{\text{Ly}\alpha} \approx f_{900}^{0.27}$). The simulated GMCs show a characteristic velocity separation of $\Delta v \approx 120 \text{ km s}^{-1}$ in the time-averaged emergent Ly α spectra, suggesting that Ly α could be useful to infer the kinematics of the interstellar and circumgalactic medium. We show that Ly α luminosities are a useful indicator of the LyC escape, provided the number of LyC photons can be deduced through stellar population modeling. Finally, we find that the correlations between the escape fractions of Ly α , ultraviolet photons at 1500Å, and the Balmer α line are weak.

Keywords: Giant molecular clouds (653) — Photoionization (2060) – Reionization (1383) – Lyman-alpha galaxies (978)

1. INTRODUCTION

Strong Lyman continuum (LyC) radiation produced by young massive stars is known to create low-density channels in giant molecular clouds (GMCs) (e.g., Dale et al. 2012; Geen et al. 2018; Kim et al. 2018; Grudić et al. 2021b). After escaping from their place of origin, the photons not only regulate the dynamics of the interstellar medium (ISM), but also drive the reionization of the Universe by ionizing neutral hydrogen in the

intergalactic space (e.g., Madau et al. 1999; Ilev et al. 2006; Mesinger & Furlanetto 2007; Gnedin 2014; Kimm & Cen 2014; Norman et al. 2015; O’Shea et al. 2015; Ocvirk et al. 2016; Pawlik et al. 2017; Rosdahl et al. 2018; Finlator et al. 2018; Doussot et al. 2019; Hutter et al. 2021). Therefore, understanding the propagation of LyC photons within GMCs is an important first step to build a coherent picture of star formation, galaxy evolution, and reionization.

Reionization theory requires a significant fraction ($\sim 10\%$) of LyC photons to escape from their host dark matter haloes in order to explain the end of reionization as well as the electron optical depth (Robertson et al.

2015; Dayal & Ferrara 2018). The escape fraction of 10% may seem low and even trivial, but this is not the case. For a simple stellar population with a Kroupa initial mass function, the majority of LyC radiation is produced by short-lived massive stars, and hence it is necessary to disrupt star-forming clouds before they evolve off the main sequence (≈ 5 Myr) to ionize the intergalactic medium (IGM). Rapidly rotating stars (Topping & Shull 2015), stars stripped of their hydrogen envelope or blue stragglers in binary systems can provide extra photons on a longer timescale (Stanway et al. 2016; Götberg et al. 2020; Secunda et al. 2020), but the disruption timescale of the GMC required is still short ($\lesssim 10$ Myr) to have high escape fractions and explain the reionization history of the Universe (e.g., Yoo et al. 2020).

Previous radiation-hydrodynamics (RHD) simulations of reionization achieved this primarily by including strong supernova (SN) feedback (e.g., Kimm & Cen 2014; Trebitsch et al. 2017). Although photoionization heating due to LyC radiation is an efficient mechanism to over-pressurize the star-forming clouds (Matzner 2002; Krumholz et al. 2007), the Stromgren sphere is usually under-resolved in galactic-scale RHD simulations. Consequently, star formation histories become more extended, and early SNe destroy star-forming clouds before young massive stars that produce the majority of ionizing radiation explode as SNe (Kimm & Cen 2014). This SN-driven escaping picture may be partly correct in that energetic explosions are required to blow out the neighboring ISM (e.g., Semenov et al. 2021). However, at least in mini-halos of mass $M_{\text{halo}} \lesssim 10^8 M_{\odot}$, radiation feedback creates low-density channels on a timescale of a few million years, allowing a large fraction ($\sim 40\%$) of the LyC radiation to escape to the IGM (Wise et al. 2014; Kimm et al. 2017; Xu et al. 2016). A recent analysis of star-forming disc galaxies also appears to suggest that local GMCs may be dispersed on a similar timescale of ~ 5 Myr, once massive stars are formed (Chevance et al. 2020; Kim et al. 2021a).

The most prominent uncertainty in the modeling of reionization originates from our lack of understanding of the earliest stage of the propagation of ionizing radiation in GMCs. Although it is becoming possible to measure the escape fraction of individual HII regions in the local galaxy (Pellegrini et al. 2012; Doran et al. 2013; McLeod et al. 2019, 2020; Della Bruna et al. 2021), the observational properties of star-forming clouds at high redshift are barely known. Moreover, simulating the evolution of GMCs is a complex task, owing to the simultaneous operation of several physical processes. Magnetic fields are known to delay gas collapse (e.g., Hennebelle & Iffrig 2014; Girichidis et al. 2018), and SNe and pre-SN feed-

back can occur simultaneously for long-lived clouds containing multiple massive stars (e.g., Lopez et al. 2014). Thus, high-resolution simulations of GMCs with a variety of initial conditions and comprehensive physical processes are very much needed.

With these motivations, Kimm et al. (2019) performed radiation-hydrodynamic simulations of GMCs with a maximum resolution of 0.25 pc, particularly focusing on the effects of the total star formation efficiency (SFE_{tot}) and spectral energy distribution of stellar populations. They found that the escape fraction of LyC photons (f_{LyC}) is generally an increasing function of time, and that f_{LyC} is higher if the binary interaction of stellar populations is taken into account or if a higher SFE_{tot} or lower metallicity is used (see also Yoo et al. 2020, for galactic-scale experiments). Independent work by Kim et al. (2019) further demonstrated that f_{LyC} decreases with an increase in the gas surface density, again confirming the increasing trend of f_{LyC} with time (c.f., Howard et al. 2018). Because the simulation duration as well as initial cloud conditions are different, direct comparisons between simulations are difficult, but the luminosity-weighted f_{LyC} tends to be very significant on cloud scales ($\sim 50\%$), which appears to be compatible with recent analyses of local HII regions (e.g., McLeod et al. 2020; Choi et al. 2020; Della Bruna et al. 2021).

Studies of the propagation of LyC radiation in GMCs are also useful to improve our understanding of the properties of the neutral medium in and around galaxies. LyC radiation that does not escape from a cloud ionizes hydrogen, which then recombines with free electrons and generates Lyman- α ($\text{Ly}\alpha$) photons with an energy of 10.2 eV. Because of its high transition probability, $\text{Ly}\alpha$ emission is one of the brightest lines in the spectrum of star-forming galaxies (Partridge & Peebles 1967), which renders it a useful tool for studying the high- z Universe (e.g., Dijkstra 2014; Ouchi et al. 2020). A neutral medium with a hydrogen column density as low as $\log N_{\text{HI}} \sim 10^{14} \text{ cm}^{-2}$ can scatter $\text{Ly}\alpha$, allowing us to probe the distribution of HI in the ISM and circumgalactic medium (CGM) (e.g., Gronke 2017; Smith et al. 2019; Song et al. 2020; Mitchell et al. 2021). Furthermore, the relative ratio of the blue part to the red part of the $\text{Ly}\alpha$ spectrum has been shown to be a good indicator of galactic inflows/outflows (e.g., Zheng & Miralda-Escudé 2002; Ahn et al. 2003; Dijkstra et al. 2006; Verhamme et al. 2006; Laursen et al. 2009; Barnes et al. 2011). Additionally, the fraction of $\text{Ly}\alpha$ emitters or the $\text{Ly}\alpha$ equivalent width distribution can be used to infer the reionization history of the Universe (e.g., Stark et al. 2011; Pentericci et al. 2011; Jung et al. 2020; Garel et al. 2021).

Of those observational findings, the detection of extended Ly α halos (Cantalupo et al. 2014; Borisova et al. 2016; Wisotzki et al. 2016; Leclercq et al. 2017) is particularly noteworthy. To explain the presence of the giant Ly α nebulae, Cantalupo et al. (2014) claimed that there may exist an unresolved neutral, clumpy CGM. Recent numerical studies have indeed pointed out that neutral clouds in galactic outflows would be found to survive longer if hydrodynamic instabilities are properly simulated on sub-parsec scales (McCourt et al. 2018; Gronke & Oh 2018; Sparre et al. 2019). Several authors further showed that an enhanced resolution of several hundred parsecs in the CGM region can better capture the thermal balance and form a large amount of neutral hydrogen (van de Voort et al. 2019; Hummels et al. 2019; Bennett & Sijacki 2020), implying that Ly α may be scattered to a greater extent in the CGM compared with the extent indicated by current theoretical predictions (e.g., Mitchell et al. 2021). The increased column density of neutral hydrogen is also likely to affect the observed f_{LyC} and the velocity separation of double peaks in the Ly α spectra (v_{sep}) in different ways, potentially providing us a useful metric to study the distribution of the ISM/CGM. On this basis, Kimm et al. (2019) compared the value of $f_{\text{LyC}-v_{\text{sep}}}$ for simulated GMCs with those for luminous compact galaxy samples and concluded that the lower v_{sep} predicted for the simulated GMCs should be attributed to the lack of interaction with the ISM/CGM. On the other hand, in their idealized simulations that mimicked GMC environments, Kakiichi & Gronke (2021) showed that the observed $f_{\text{LyC}-v_{\text{sep}}}$ could be reproduced if turbulent structures were well maintained. Given that the simulation setups of the two studies are idealized, theoretical experiments modeling the emergence of Ly α in realistic settings are thus required to examine if $f_{\text{LyC}-v_{\text{sep}}}$ can be used to study the distribution of neutral hydrogen in the ISM/CGM and to physically interpret the observed Ly α properties of galaxies.

Because Ly α emission is mainly produced by recombination (e.g., Kimm et al. 2019), all processes that ionize hydrogen, such as photoionization or collisional shocks, should be included in simulations of Ly α radiative transfer. Early works that did not solve the fully coupled radiation-hydrodynamic equations assumed Ly α sources with constant line broadening (Verhamme et al. 2012) or computed the emission by post-processing outputs of hydrodynamic simulations (Yajima et al. 2014; Smith et al. 2019; Byrohl et al. 2021). The finite resolution of galaxy-scale simulations (~ 10 – 100 pc) was also a limiting factor. However, the use of the zoom-in technique in cosmological simulations and simulations of ISM patches

are now making it possible to investigate the evolution of Ly α equivalent widths (Smith et al. 2019) or the effects of cosmic ray-driven winds on Ly α profiles at sub-parsec resolutions (Gronke et al. 2018). Nevertheless, there is a lack of simulations modeling Ly α sources directly from GMCs or the ISM (Kimm et al. 2019; Kakiichi & Gronke 2021). In order to measure the escape of LyC radiation and to understand the emerging characteristic spectra of GMCs, we perform a suite of radiation-magneto-hydrodynamic (RMHD) simulations with a maximum of 0.02–0.08 pc resolution, including stellar feedback due to ionizing radiation and SN explosions. Improving upon the work of Kimm et al. (2019), we model star formation by self-consistently computing the formation and accretion on sink particles and include the effects of magnetic fields. Apart from spherical clouds, we also simulate filamentary or homogeneous clouds to examine the effect of morphology on the emergence of LyC and Ly α photons.

This paper is organized as follows. We describe the initial conditions and physical processes included in numerical simulations in Section 2. A Monte Carlo radiative transfer method for Ly α and a simple ray tracing method for LyC radiation are also presented. In Section 3, we analyze the dependence of escape fractions and emergent Ly α profiles on GMC properties, and in Section 4, we discuss the main parameter controlling the escape of LyC radiation and compare the escape of LyC and Ly α photons with that of UV radiation at 1500Å and Balmer α (H α) photons. Finally, we summarize our primary findings and present our conclusions in Section 5.

2. METHODOLOGY

In this section, we describe our suite of RMHD simulations in which the evolution of GMCs is modelled with various initial conditions. We also present radiative transfer methods used to compute the propagation of LyC and Ly α photons.

2.1. Numerical simulations

We perform 18 idealized simulations of GMCs¹ with the adaptive mesh refinement code, RAMSES (Teyssier 2002). The magneto-hydrodynamic equations are solved using the Harten-Lax-van Leer-Discontinuity Riemann solver with a constrained transport scheme (Fromang et al. 2006). The Poisson equation is evolved with the particle-mesh method (Guillet & Teyssier 2011), and radiation transport is modelled using a moment-based method with the M1 closure relation for the Eddington

¹ These simulations are part of the PRALINES project (Bieri et al. *in prep.*).

tensor (Rosdahl et al. 2013). We adopt a Courant factor of 0.8. Physical processes considered in the simulations are identical to those of Geen et al. (2018), except that SN explosions are also included in the current study. Interested readers are referred to Geen et al. (2018) for details of the initial conditions, and we recapitulate the main features below.

We simulate GMCs with different gas masses (10^5 [M5] or $10^6 M_\odot$ [M6]), surface densities (typical versus dense [D]), metallicities (low [Z002] or high [Z014]), resolutions (low [LR], high [HR]), input physics (SN), magnetic field strengths (B), turbulence strength (T), and morphology (spherical [S], filamentary [F], homogeneous [H]), as outlined in Table 1 and Figure 1. The clouds initially comprise two layers of gas distributions with different densities, which are chosen by considering the total mass ($M_{\text{cl}} = 10^5$ or $10^6 M_\odot$) and the typical average surface density of observed GMCs ($\Sigma \sim 100\text{--}200 M_\odot \text{pc}^{-2}$) or the dense case ($650 M_\odot \text{pc}^{-2}$) (Figure 2). The region inside $r < 20$ pc (10.8 pc for M5) is modelled as a Bonnor-Ebert sphere with scaling core radius of $R_c = 6.6$ pc (3.6 pc for M5), such that $\rho(r) \propto R_c^2/(R_c^2 + r^2)$, which we refer to as an “isothermal” density profile. The outer sphere has a constant hydrogen number density of $n_{\text{H}} = 50 \text{ cm}^{-3}$ up to 40 pc ($n_{\text{H}} = 30 \text{ cm}^{-3}$ up to 21.6 pc for M5). The background density is set to be $n_{\text{H}} \approx 1 \text{ cm}^{-3}$. Initial turbulent velocity fields with random phases are created using a Kolmogorov power spectrum, and we relax them for $0.5 t_{\text{ff}}$ without gravity, where t_{ff} is the free-fall timescale. Self-gravity is turned on after $0.5 t_{\text{ff}}$. The initial conditions for filamentary clouds are generated by adopting identical velocity fields for the x- and y- directions. For homogeneous clouds, we do not use double gas profiles, but simply adopt a sphere of uniform density $n_{\text{H}} = 117 \text{ cm}^{-3}$.

The simulated volume is covered with 128^3 coarse cells (level 7), which are further refined up to level 11–13. The corresponding maximum resolution ranges from $\Delta x_{\text{min}} = 0.02\text{--}0.08$ pc (Table 1). Note that the adopted cell width is 3–10 times smaller than that used by Kimm et al. (2019). Refinement continues until the maximum level is reached if the local Jeans length is resolved by fewer than 10 cells or the mass of a cell exceeds $0.27 M_\odot$. Cells that contain a sink particle or are within the accretion radius of a sink particle ($4\Delta x_{\text{min}}$) are also maximally refined.

We model the formation of sink particles representing stars in dense regions where gas collapse occurs along the three axes, as described in Bleuler & Teyssier (2014). The clump finder first identifies dense clumps using a watershed algorithm, and places a sink particle of mass $0.001 M_\odot$ in a virialized, dense cell if

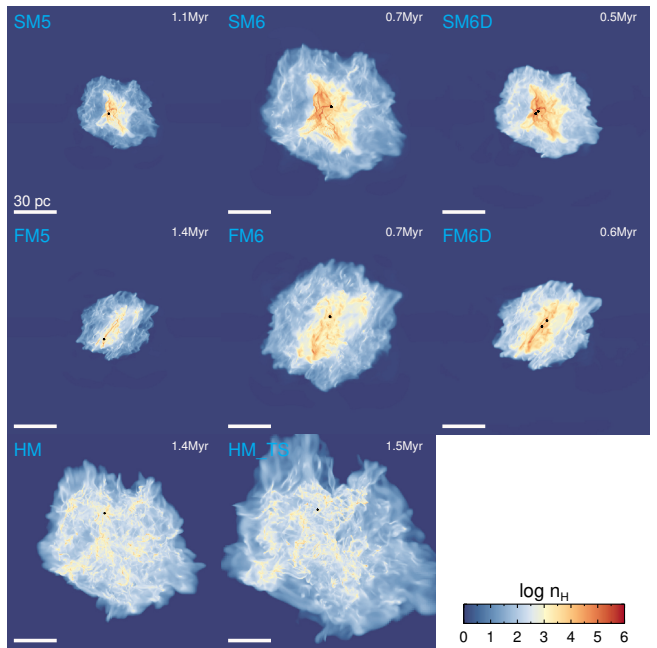


Figure 1. Projected density distributions of the simulated clouds when the first star particle(s) are formed. The clouds have different morphologies (S: spherical, F: filamentary, H: homogeneous), masses (M5: 10^5 , M6: $10^6 M_\odot$), surface densities (D: dense), and turbulence (TS: strong turbulence). The images measure 150 pc on a side, and the black dot indicates the position of the star particles.

$n_{\text{H}} \geq n_{\text{th,sink}}$. The critical density for sink formation is chosen as $n_{\text{th,sink}} \geq 881 \text{ cm}^{-3}/(\Delta x_{\text{min}}/\text{pc})^2$, motivated by the Jeans criterion. For example, $n_{\text{th,sink}}$ in the fiducial M6 clouds with $\Delta x_{\text{min}} = 0.08$ pc is $1.47 \times 10^5 \text{ cm}^{-3}$. Accretion onto the sink particle is modelled using a threshold such that 75% of the mass above $n_{\text{th,sink}}$ is transferred to the sink in each time step (Bleuler & Teyssier 2014). Star particles are then created based on a pre-determined list of the masses of individual stars, which is randomly sampled assuming a Chabrier initial mass function (Chabrier 2003). Note that we use the pre-determined list for reproducibility of the simulations and also to facilitate the comparison of simulations with different parameters. We assume that every time a sink particle accretes more than $120 M_\odot$, a massive star of mass between $8 \leq m \leq 120 M_\odot$ is formed and moves with the sink particle. The rest of the stellar mass is assumed to be non-radiating.

Radiative cooling due to primordial and metallic species is modelled on the basis of temperature, density, and metallicity. Metallicity-dependent gas cooling above 10^4 K is included by using piece-wise fits to Sutherland & Dopita (1993). For metal cooling at lower temperatures, we consider fine structure transitions of CII and OI, as described in Audit & Hennebelle (2005). By con-

Table 1. Initial conditions and parameters used in the simulations. From left to right, the columns indicate (1) the simulation label, (2) cloud mass, (3) average gas surface density of the entire (inner) cloud, (4) radius of the entire (inner) cloud, (5) shape, (6) gas metallicity, (7) size of the simulated box, (8) size of the finest AMR cells, (9) volume-weighted plasma beta ($\beta_P \equiv P_{\text{th}}/P_{\text{mag}}$) at t_{relax} , (10) inclusion of photoionization heating, (11) inclusion of Type II SN explosions, (12) one-dimensional velocity dispersion at t_{relax} , and (13) time of the final snapshot.

Name	M_{cloud} [M_{\odot}]	Σ_{gas} [M_{\odot}/pc^2]	r_{cloud} [pc]	Shape	Z_{gas}	L_{box} [pc]	Δx_{min} [pc]	β_P	PH	SN	$\sigma_{1d,0}$ [km s^{-1}]	t_{final} [Myr]
(1)	(2)	(3)	(4)	(5)	(6)	(7)	(8)	(9)	(10)	(11)	(12)	(13)
SM5_pZ002	1.4×10^5	93 (274)	21.6 (10.8)	Spherical	0.002	173	0.04	0.31	✓	–	2.9	8.4
SM5_pZ014	1.4×10^5	93 (274)	21.6 (10.8)	Spherical	0.014	173	0.04	0.31	✓	–	2.9	8.4
SM5_pZ002_BW	1.4×10^5	93 (274)	21.6 (10.8)	Spherical	0.002	173	0.04	2.89	✓	–	2.9	8.4
SM5_pZ002_BS	1.4×10^5	93 (274)	21.6 (10.8)	Spherical	0.002	173	0.04	0.03	✓	–	2.9	8.4
SM5_pZ002_HR	1.4×10^5	93 (274)	21.6 (10.8)	Spherical	0.002	173	0.02	0.31	✓	–	2.9	8.4
SM5_pZ002_LR	1.4×10^5	93 (274)	21.6 (10.8)	Spherical	0.002	173	0.08	0.31	✓	–	2.9	8.4
FM5_pZ002	1.4×10^5	93 (274)	21.6 (10.8)	Filamentary	0.002	173	0.04	0.31	✓	–	2.8	8.4
SM6_pZ002	1.4×10^6	278 (820)	39.6 (19.8)	Spherical	0.002	317	0.08	0.11	✓	–	7.4	8.3
SM6_sZ002	1.4×10^6	278 (820)	39.6 (19.8)	Spherical	0.002	317	0.08	0.11	✓	✓	7.4	8.3
SM6_sZ014	1.4×10^6	278 (820)	39.6 (19.8)	Spherical	0.014	317	0.08	0.11	✓	✓	7.4	8.3
SM6_sZ002_HR	1.4×10^6	278 (820)	39.6 (19.8)	Spherical	0.002	317	0.04	0.11	✓	✓	7.4	8.3
FM6_sZ002	1.4×10^6	278 (820)	39.6 (19.8)	Filamentary	0.002	317	0.08	0.11	✓	✓	6.8	8.3
SM6D_pZ002	1.4×10^6	647 (1905)	26.0 (13.0)	Spherical	0.002	208	0.05	0.01	✓	–	7.4	8.4
SM6D_pZ014	1.4×10^6	647 (1905)	26.0 (13.0)	Spherical	0.014	208	0.05	0.01	✓	–	7.4	8.3
SM6D_sZ002	1.4×10^6	647 (1905)	26.0 (13.0)	Spherical	0.002	208	0.05	0.01	✓	✓	7.4	8.3
FM6D_sZ002	1.4×10^6	647 (1905)	26.0 (13.0)	Filamentary	0.002	208	0.05	0.01	✓	✓	7.2	8.3
HM6_sZ002	10^6	200	40	Homo-sph	0.002	320	0.08	0.24	✓	✓	5.5	8.3
HM6_sZ002_TS	10^6	200	40	Homo-sph	0.002	320	0.08	0.11	✓	✓	10.0	8.3

trast, we solve the non-equilibrium chemistry for the primordial species (H, and He), which is coupled with the local radiation field produced by each star particle (Rosdahl et al. 2013), in order to accurately account for photoionization heating. Stellar spectra are taken from the rotating stellar evolution model of the Geneva tracks (Ekström et al. 2012; Georgy et al. 2013) and are used to calculate the time-dependent emissivity of ionizing radiation. In this study, we adopt three radiation bins (13.6–24.59 eV, 24.59–54.42 eV, and 54.42 eV– ∞).

When massive stars evolve off the main sequence and explode as SN, we inject a thermal energy of 10^{51} erg into 27 neighboring cells of the sink particle. This method is often incapable of resolving the local cooling length and under-estimates the impact of explosions in dense environments. However, the inclusion of the radiation field and photoionization feedback decreases the density into which SNe explode (Krumholz et al. 2007), and we verify that the local cooling radius is sufficiently resolved by more than three resolution elements by the time a SN explodes (Kim & Ostriker 2015).

Magnetic fields are initially aligned in the x -direction, and then evolved following turbulent gas motions. The initial magnetic field strengths are set by considering

the Alfvén crossing time $t_A \equiv r_c \sqrt{\rho_{\text{max},i}}/B_{\text{max},i}$, where $\rho_{\text{max},i}$ is the initial maximum density of the cloud and $B_{\text{max},i}$ is the initial maximum magnetic field strength. The volume-weighted magnetic field strengths of spherical clouds with low surface density (SM5 and SM6) are ≈ 7 and $\approx 12 \mu G$, respectively, while for the SM6D models they are $\approx 45 \mu G$. A less massive cloud with weak (BW) or strong magnetization (BS) has a magnetic field strength of $\approx 2 \mu G$ or $23 \mu G$, respectively. Furthermore, filamentary clouds with the same mass and surface density are set to have nearly the same magnetic field strengths. HM6 models with weak and strong turbulence (HM6_sZ002 and HM6_sZ002_TS) have a volume-weighted magnetic field strength of $\approx 5 \mu G$. The corresponding plasma beta (β_P), given by $P_{\text{th}}/P_{\text{mag}}$, is presented in Table 1, where P_{th} and P_{mag} are the thermal and magnetic pressure, respectively.

Simulations are run until $t \approx 8.4$ Myr, at which point the majority of gas is ionized and star formation is completed. Each run produces approximately 100–130 snapshots at intervals of $\Delta t \lesssim 0.1$ Myr.

2.2. Monte Carlo Ly α radiative transfer

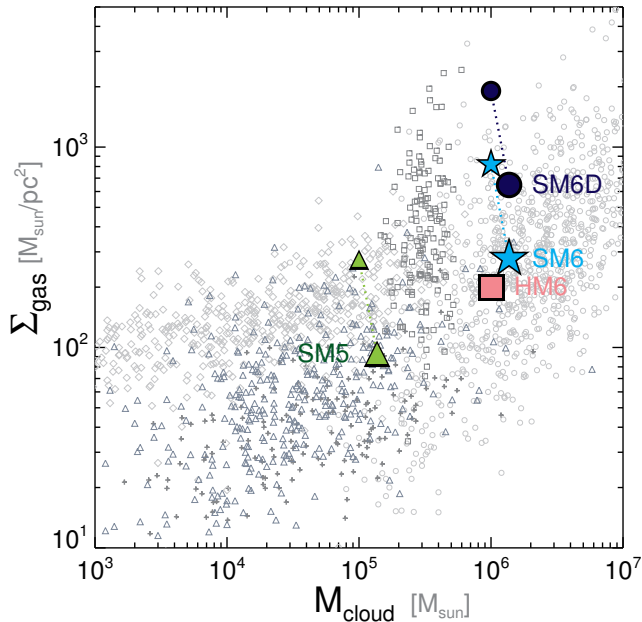


Figure 2. Properties of the simulated GMCs. The cloud mass and surface density are displayed twice except for the homogeneous cloud (HM6), depending on whether the gas inside the inner (smaller) or outer layer (larger symbols) of the cloud is included. Filamentary clouds share the same initial conditions as spherical clouds (SM). The properties of the observed GMCs are shown as grey symbols: Heyer et al. (2009, crosses), Roman-Duval et al. (2010, diamonds), Wong et al. (2011, triangles), Colombo et al. (2014, circles), Liu et al. (2021, squares)

To compute Ly α profiles, we post-process our simulation outputs with the Monte Carlo Ly α radiative transfer code RASCAS (Michel-Dansac et al. 2020). We generate 10^5 Ly α photon packets in ionized regions via collisional excitation followed by de-excitation or recombinative radiation, as outlined in Kimm et al. (2019). The emission rates in each gas cell are calculated from the temperature, density, and ionization fractions obtained from our RMHD simulations. Note that LyC photons that escape from the simulated GMCs are not included as a source term in the calculation of Ly α radiative transfer. The initial frequency of the photons is determined from the gas motion, and we shift it by $x_{\text{ran}}\Delta\nu$, where $\Delta\nu$ is the Doppler broadening due to the thermal motion and x_{ran} is a random number drawn from the Gaussian distribution with the standard deviation of 1. Ly α photons are then resonantly scattered by neutral hydrogen and undergo diffusion in space and frequency. To reduce the computational cost, we use a core skipping algorithm (Smith et al. 2015). We also include the recoil effect and transition due to a small amount of deuterium ($D/H = 3 \times 10^{-5}$).

The most significant uncertainty in our modeling of Ly α radiative transfer comes from the determination of the amount of dust, for which we follow the method of Laursen et al. (2009), as

$$n_{\text{dust}} = (n_{\text{HI}} + f_{\text{dust}}^{\text{ion}} n_{\text{HII}}) Z/Z_{\text{ref}}. \quad (1)$$

Here n_{dust} is the pseudo number density of dust, n_{HI} and n_{HII} are the number density of neutral and ionized hydrogen, and $f_{\text{dust}}^{\text{ion}}$ is a free parameter that controls the amount of dust in ionized media; we take $f_{\text{dust}}^{\text{ion}} = 0.01$ (Laursen et al. 2009). Z_{ref} is a parameter that determines the overall dust mass relative to hydrogen. We take $Z_{\text{ref}} = 0.005$ with an albedo (\mathcal{A}) of 0.32 for low-metallicity runs, while $Z_{\text{ref}} = 0.02$ and $\mathcal{A} = 0.325$ are used for metal-rich cases (Weingartner & Draine 2001). Dust absorption cross-sections for the low- and high-metallicity runs are taken from the dust models of the Small Magellanic Cloud (SMC) and Milky Way (MW) presented by Weingartner & Draine (2001), respectively.

2.3. Measurement of LyC escape

We measure the escape fraction of LyC radiation by computing the optical depth in 12,288 directions from each star particle using the HEALPIX algorithm with $N_{\text{side}} = 32$ (Górski et al. 2005). The optical depth associated with primordial species is calculated by assuming that the ionizing radiation is absorbed by neutral hydrogen, singly ionized helium (Osterbrock & Ferland 2006), and neutral helium (Yan et al. 2001). Attenuation due to dust is modeled using the SMC-type absorption coefficient for the runs with $Z = 0.002$ or MW-type coefficient for the runs with $Z = 0.014$ (Weingartner & Draine 2001). We do not include absorption by molecular hydrogen as its formation and destruction are not modeled explicitly in this study. Moreover, neglecting absorption by molecular hydrogen is unlikely to change the escape fraction of LyC photons significantly, as its optical depth is an order of magnitude smaller than that of neutral hydrogen (see Figure 5 of Kimm et al. 2019).

3. RESULTS

In this section, we analyze the general evolutionary features of our fiducial cloud, present the systematic analysis on the escape of LyC and Ly α photons, and discuss the shape of Ly α spectra predicted from GMCs with different physical properties.

3.1. General evolutionary features

Figure 3 (top row) shows the general evolution of the density distribution and emergent Ly α profiles of our fiducial cloud of mass $10^6 M_{\odot}$ and metallicity of $Z = 0.002$ (SM6_sZ002). The initially driven turbulence

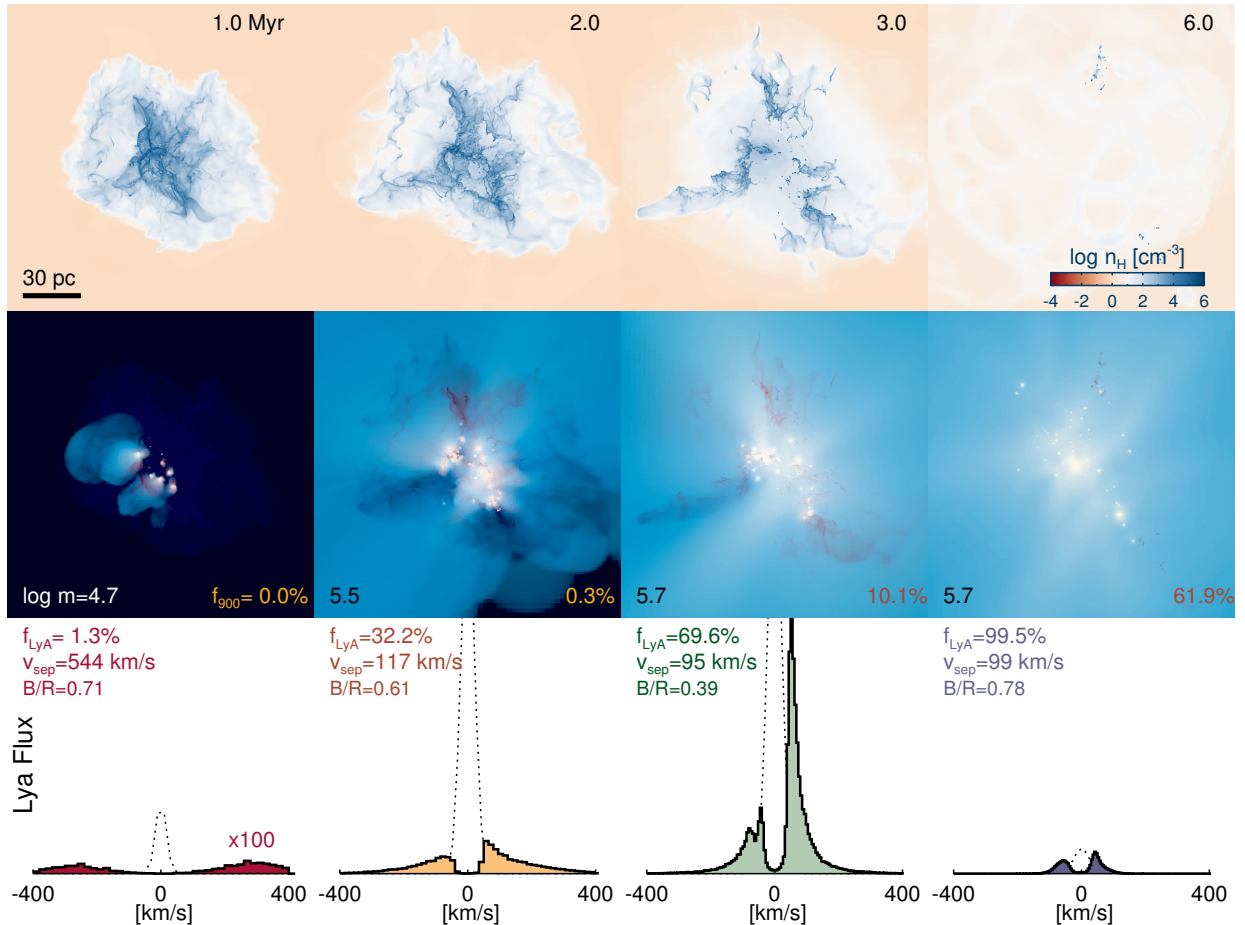


Figure 3. Evolution of a GMC of mass $10^6 M_{\odot}$ and metallicity of 0.002 (SM6_sZ002). The top panels depict projected distributions of the density, and the middle panels show composite images of the density, the fraction of ionized hydrogen, and HI-ionizing photon flux in the central region (158 pc on a side) of the simulation. The intrinsic (dotted) and emergent (solid) spectra of Ly α photons are shown in the bottom panels. The emergent velocity profile of the leftmost column is magnified by a factor of 100 to improve readability. The simulation epoch is displayed in the upper right corner of the figures in the top row. The two values in the middle-row panels indicate the logarithmic total mass of stars and the escape fraction at $\lambda = 900 \text{ \AA}$. In the bottom panels, we also include the escape fraction, the velocity separation of the two peaks, and the flux ratio of the blue part to the red part of the Ly α spectrum.

in the GMC leads to the formation of filamentary structures, which then collapse to form sink particles (we re-iterate that these do not represent individual stars). Since there is no continuous energy input to act against gravity, gas accretes efficiently onto sink particles and a number of massive stars emerge within a short timescale of 1–2 Myr. By $t = 3 \text{ Myr}$, approximately 50 per cent of the cloud mass is converted into stars (Figure 4), and strong UV radiation photoheats and expels gas from the cloud.

As previously noted in the literature (Dale et al. 2012; Howard et al. 2018; Kimm et al. 2019; He et al. 2020; Yoo et al. 2020; Kim et al. 2021b), the escape of LyC photons is regulated by the evolution of the GMCs (middle row). In the early phase of star formation, no LyC photon escapes from the clouds. However, a significant

fraction ($\gtrsim 10\%$) of the ionizing radiation leaks from the cloud, once the cloud is disrupted because of photoionization feedback. By $t = 8.3 \text{ Myr}$, 42.0 per cent of the ionizing radiation generated until then escapes from the fiducial cloud with a total SFE_{tot} of 0.51. If we further count photons that would be produced during $8.31 < t \leq 20 \text{ Myr}$ and assume that the escape fraction is kept the same as the value at the last snapshot (i.e. $f_{\text{LyC}} = 64\%$), the luminosity-weighted escape fraction would increase only slightly to $\langle f_{\text{LyC}} \rangle_{20 \text{ Myr}} = 42.3\%$, as only a small fraction ($\approx 2\%$) of the total number of LyC photons is generated after $t = 8.31 \text{ Myr}$ in the stellar evolution model adopted in this study.

Similarly, the escape fraction of Ly α photons ($f_{\text{Ly}\alpha}$) increases with the disruption of the cloud, but the escape is systemically more efficient than that of LyC ra-

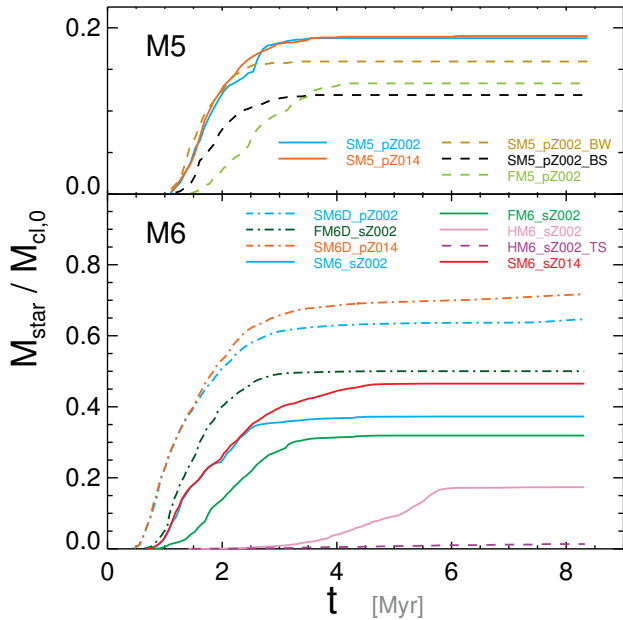


Figure 4. Star formation histories of the simulated GMCs. Different color-codes and line styles correspond to runs with different initial conditions and input physics, as indicated in the legend. In most of the clouds, star formation ends within about 3 Myr, except for the homogeneous spherical clouds in which gas collapses slowly because of its lower surface density.

diation. This is not surprising, given that Ly α photons are not destroyed but scattered by neutral hydrogen. We also note that the typical properties of Ly α -emitting gas change rapidly within the timescale of a few Myr. During the early phases of cloud evolution, most of the Ly α photons are produced in dense ($n_{\text{H}} \approx 10^{3.5-4.5} \text{ cm}^{-3}$) and warm ($T \approx 10^{4.1} \text{ K}$) gas. By contrast, the density is reduced to $n_{\text{H}} \sim 5\text{--}10 \text{ cm}^{-3}$ when most of the GMC is dispersed. More interesting is the large number of scattering events which results in a significant velocity shift in the Ly α profile. As evident in the bottom panels of Figure 3, the separation of the two velocity peaks (v_{sep}) is as large as $\sim 500 \text{ km s}^{-1}$ in the early phase. Once the dense clumps enshrouding young massive stars are ionized and destroyed, Ly α photons are scattered less and v_{sep} decreases to $\approx 100 \text{ km s}^{-1}$. Expanding motion of the cloud rapidly develops because of photoionization feedback (e.g., Rosdahl & Teyssier 2015; Geen et al. 2017; Kim et al. 2018; Grudić et al. 2021b), and back-scattered Ly α photons are preferentially observed (Verhamme et al. 2006; Dijkstra et al. 2006). Even when the cloud becomes optically thin to LyC radiation ($t = 6 \text{ Myr}$), v_{sep} does not fall below $\sim 100 \text{ km s}^{-1}$, as the Ly α photons are still scattered by the residual neutral hydrogen present in the expanding cloud.

In the simulation, starting from the first SN that explodes at $t = 4.5 \text{ Myr}$, a total of 438 SNe explode, blowing away the ambient medium. These explosions not only provide thermal energy but also re-distribute mass from stars to gas, sporadically enhancing the neutral fraction of hydrogen via radiative cooling. Moreover, our adopted stellar evolution model predicts a relatively short period ($\sim 5 \text{ Myr}$) of bright phases in LyC because rejuvenation through binary interaction is neglected. Consequently, a small fraction ($\sim 0.1\text{--}1\%$) of neutral hydrogen persists in the dispersed bubbles and 40 per cent of LyC photons are still absorbed at $t \approx 8 \text{ Myr}$. We expect the absorption by residual neutral hydrogen to be suppressed once a sufficient number of SNe explode and blow out most of the gas in the GMC.

We note that the simulated cloud shows the brightest Ly α emission in the intermediate stage, during which only a portion of the cloud is disrupted (third column in Figure 3). Although $f_{\text{Ly}\alpha}$ is close to unity in later stages, the recombinative emission channel is not efficient because the cloud is already dispersed and few LyC photons are converted into Ly α . However, if sufficient LyC photons continue to escape from the cloud, Ly α photons will be produced in the ISM, leading to a significant change in the emergent Ly α spectrum, as discussed in Kimm et al. (2019, Figure 14).

3.2. Effects of physical properties on the escape of LyC and Ly α

We now investigate how different physical properties of a cloud affect the propagation of LyC and Ly α photons. We first show the star formation histories of our various clouds, which are essentially driven by free-fall collapse, in Figure 4. We then compare the escape fractions for different cloud masses, surface densities, metallicities, magnetic fields, morphologies, and turbulent strengths in Figures 5–6. The effects of resolution are discussed in Appendix A. The luminosity-weighted escape fractions are summarized in Table 2 and shown in Figure 7 for a convenient overview.

3.2.1. Cloud mass

Our simulated GMCs with a mass of $10^5 M_{\odot}$ tend to have a relatively low SFE_{tot} of ≈ 0.19 , independent of the metallicity (SM5_pZ002 or SM5_pZ014). By contrast, more massive clouds (SM6_sZ002 and SM6_sZ014) exhibit a higher SFE_{tot} of $\approx 0.3\text{--}0.5$. The mass dependence partly arises because it takes more time to photoionize and destroy more massive clouds for a given SFE_{tot} and density, since they are larger in size (e.g., Kimm et al. 2019, see their Appendix A). The higher SFE_{tot} also result from the higher gas surface density considered for massive clouds ($\Sigma = 278$ versus $93 M_{\odot} \text{ pc}^{-2}$);

Table 2. Escape fractions at various wavelengths. From left to right, the columns indicate the name of the simulation, (1) simulation time in Myr, (2) SFE_{tot} , (3) escape fraction of LyC radiation, (4) extrapolated escape fraction obtained by assuming that f_{LyC} in the final snapshot is maintained constant until 20 Myr, (5) escape fraction of photons at [880, 912] Å, (6) escape fraction of Ly α photons, (7) escape fraction of photons at [1475, 1525] Å, (8) escape fraction of H α photons, (9) intrinsic UV magnitude at 1500 Å, (10) intrinsic Ly α luminosity in units of erg s^{-1} , (11) intrinsic H α luminosity in units of erg s^{-1} , and (12) destruction timescale (t_{desc}) in Myr. The escape fractions are luminosity-weighted over the entire simulation duration, whereas $\langle M_{1500} \rangle$, $\langle L_{\text{Ly}\alpha} \rangle$, and $\langle f_{\text{H}\alpha} \rangle$ are the average during t_{desc} from the onset of star formation. The parameter t_{desc} is defined by the moment at which a gas mass denser than 100 cm^{-3} is reduced by 90% relative to its initial value.

Name	t_{final}	SFE_{tot}	$\langle f_{\text{LyC}} \rangle$	$\langle f_{\text{LyC}} \rangle_{20}$	$\langle f_{900} \rangle$	$\langle f_{\text{Ly}\alpha} \rangle$	$\langle f_{1500} \rangle$	$\langle f_{\text{H}\alpha} \rangle$	$\langle M_{1500} \rangle$	$\langle L_{\text{Ly}\alpha} \rangle$	$\langle L_{\text{H}\alpha} \rangle$	t_{desc}
	(1)	(2)	(3)	(4)	(5)	(6)	(7)	(8)	(9)	(10)	(11)	(12)
SM5_pZ002	8.4	0.188	0.690	0.690	0.629	0.711	0.946	0.833	-10.9	39.6	38.6	2.7
SM5_pZ014	8.4	0.190	0.574	0.569	0.537	0.553	0.878	0.643	-10.9	39.7	38.8	3.0
SM5_pZ002_BW	8.4	0.159	0.656	0.657	0.598	0.738	0.948	0.879	-10.7	39.6	38.7	2.4
SM5_pZ002_BS	8.4	0.119	0.524	0.519	0.430	0.719	0.931	0.908	-10.5	39.5	38.6	3.0
SM5_pZ002_HR	8.4	0.174	0.659	0.660	0.595	0.725	0.939	0.841	-10.7	39.6	38.6	2.7
SM5_pZ002_LR	8.4	0.140	0.620	0.620	0.544	0.765	0.954	0.927	-10.6	39.5	38.6	2.9
FM5_pZ002	8.4	0.133	0.635	0.641	0.545	0.844	0.957	0.939	-10.3	39.4	38.5	2.9
SM6_pZ002	8.3	0.374	0.441	0.444	0.404	0.523	0.843	0.728	-14.1	41.1	40.1	3.1
SM6_sZ002	8.3	0.373	0.420	0.423	0.378	0.542	0.843	0.740	-14.1	41.1	40.1	3.1
SM6_sZ014	8.3	0.465	0.342	0.360	0.358	0.299	0.653	0.427	-14.3	41.3	40.3	4.2
SM6_sZ002_HR	8.3	0.401	0.327	0.332	0.295	0.436	0.755	0.632	-14.3	41.2	40.2	3.5
FM6_sZ002	8.3	0.319	0.466	0.468	0.399	0.556	0.866	0.751	-13.8	41.0	40.0	3.6
SM6D_pZ002	8.4	0.647	0.192	0.192	0.165	0.360	0.563	0.623	-14.7	41.4	40.4	3.0
SM6D_pZ014	8.3	0.717	0.258	0.260	0.255	0.218	0.514	0.468	-14.6	41.4	40.5	3.0
SM6D_sZ002	8.3	0.631	0.302	0.311	0.207	0.354	0.597	0.584	-14.7	41.4	40.4	3.5
FM6D_sZ002	8.3	0.500	0.363	0.370	0.328	0.450	0.793	0.718	-14.4	41.3	40.3	2.9
HM6_sZ002	8.3	0.174	0.576	0.633	0.497	0.657	0.879	0.799	-12.1	40.3	39.3	4.6
HM6_sZ002_TS	8.3	0.013	0.391	0.448	0.300	0.852	0.873	0.954	-9.6	39.3	38.3	4.5+

this is discussed in the following subsection (Sec. 3.2.2). On the other hand, the inclusion of SN explosions does not change a SFE_{tot} dramatically (SM6_pZ002 versus SM6_sZ002), as they occur after photoionization feedback destroys the cloud (see also Grudić et al. 2021b).

Despite the higher SFE_{tot} , a smaller fraction of LyC and Ly α photons escape from massive GMCs. As shown in Figure 5-(a), the escape fractions reach almost unity in both the $10^5 M_{\odot}$ and $10^6 M_{\odot}$ clouds, but the rise in f_{LyC} is much slower in the massive one because of the slow disruption. In total, our fiducial GMC (SM6_pZ002) shows a luminosity-weighted escape fraction of $\langle f_{\text{LyC}} \rangle = 44.1\%$, whereas 69.0% of LyC radiation leaks from the less massive cloud (SM5_pZ002). Similarly, we obtain $\langle f_{\text{Ly}\alpha} \rangle = 52.3\%$ and 71.1% for these clouds, respectively, ignoring the Ly α photons that would be potentially produced in the ISM by the leaking LyC radiation (Figure 6-(a)).

Our results are consistent with previous findings. Dale et al. (2012) computed the escape fraction of LyC radiation from metal-rich clouds with various sizes and turbulence for $2\text{--}3t_{\text{ff}}$. Their run ‘D’ was similar to our

SM5 series in that the velocity dispersion was low and feedback was efficient. In their run, the resulting escape fraction of LyC radiation within ≈ 20 Myr was 70%, similar to our predictions. In Dale et al. (2013), the massive cloud of mass $10^6 M_{\odot}$ (UZ) showed an escape fraction of 23%. However, this measurement was performed within 3 Myr, which implies that the final escape fraction could be higher, consistent with our predictions. Kimm et al. (2019) and He et al. (2020) also found that the escape fractions of LyC and Ly α photons were higher in less massive clouds.

3.2.2. Gas surface density

Now we turn to the impact of the gas surface density on the escape of LyC and Ly α radiation. As shown in Figure 2, our fiducial massive GMCs have a surface density (Σ_{gas}) of $278 M_{\odot} \text{ pc}^{-2}$, motivated by observations of GMCs in M51 (e.g., Colombo et al. 2014). However, GMCs with a higher surface density are also observed (e.g., Liu et al. 2021) and hence we compare to simulations with a higher surface density of $\Sigma_{\text{gas}} = 647 M_{\odot} \text{ pc}^{-2}$.

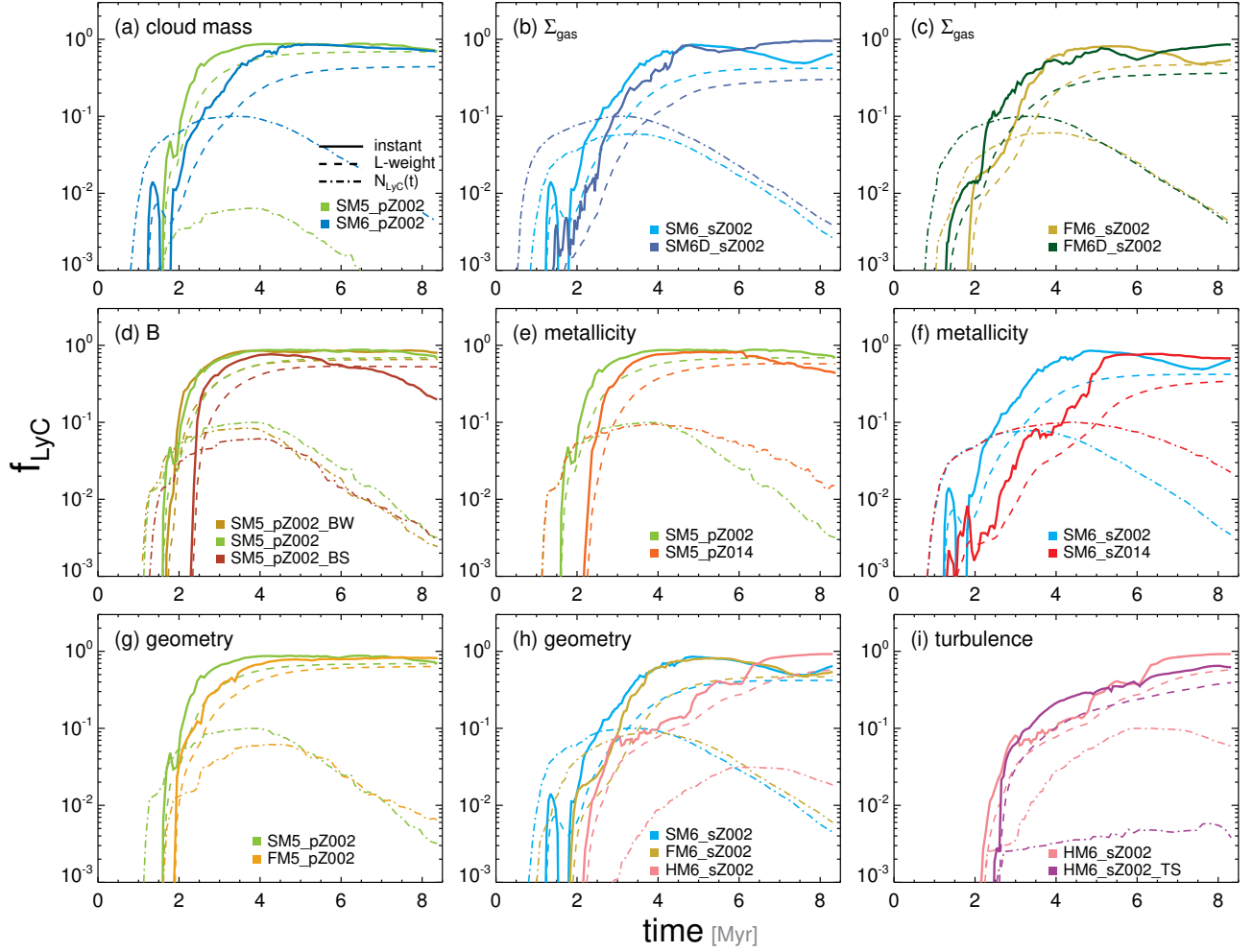


Figure 5. Escape fraction of LyC photons (f_{LyC}) in GMCs simulated with different input physics and parameters. The solid and dashed lines indicate instantaneous and luminosity-weighted escape fractions, respectively, and the dot-dashed lines show the intrinsic number of LyC photons (N_{LyC}). Note that the maximum N_{LyC} is normalized to 0.1 in each panel for better readability. The different panels compare the escape fraction from different runs, which are indicated in the legend. The escape fraction generally increases with time since the GMC gets disrupted.

We find that star formation commences earlier in denser GMCs (SM6D_sZ002 or FM6D_sZ002) compared with GMCs with the fiducial surface density (Figure 5-(b) and (c)). While the denser clouds collapse more rapidly because of their shorter free-fall timescale, it takes longer for the LyC photons to escape from the cloud. Since the cloud mass is set to be the same in the runs with different surface densities, denser clouds are smaller in size, and the high density around young stars prevents the ionization front from expanding efficiently. As a result, despite extreme SFE_{tot} of (0.631, 0.500), only (30.2%, 36.3%) of the LyC photons escape from the (SM6D_sZ002, FM6D_sZ002) runs, respectively. Such negative dependence on the gas surface density was also observed by Kim et al. (2019) from an analysis of RHD simulations of turbulent GMCs of mass 10^4 –

$10^6 M_{\odot}$ (see also He et al. 2020, for smaller and higher density clouds).

Similarly, the escape of Ly α photons is less efficient in dense clouds. While more than half of the Ly α photons leak from the clouds with the fiducial Σ_{gas} , $\langle f_{\text{Ly}\alpha} \rangle$ is reduced to $\approx 1/3$ in the dense cloud cases. Although not shown in Figures 5 and 6, we also compute the evolution of a dense, metal-rich cloud without SNe (SM6D_pZ014), where the number of stars formed is the largest (SFE_{tot} = 0.717). In spite of the high SFE_{tot}, the cloud shows the lowest $\langle f_{\text{Ly}\alpha} \rangle$ of 21.8%, which is even smaller than that $\langle f_{\text{Ly}\alpha} \rangle$ of the SM6D_sZ002 run by a factor of ≈ 1.5 . These low $\langle f_{\text{Ly}\alpha} \rangle$ results are intriguing, given that observations of local starbursts sometimes reveal a high $f_{\text{Ly}\alpha}$ exceeding 50% (e.g., Verhamme et al. 2017). Although a direct inference should be drawn with caution, our experiments suggest that such a high $f_{\text{Ly}\alpha}$

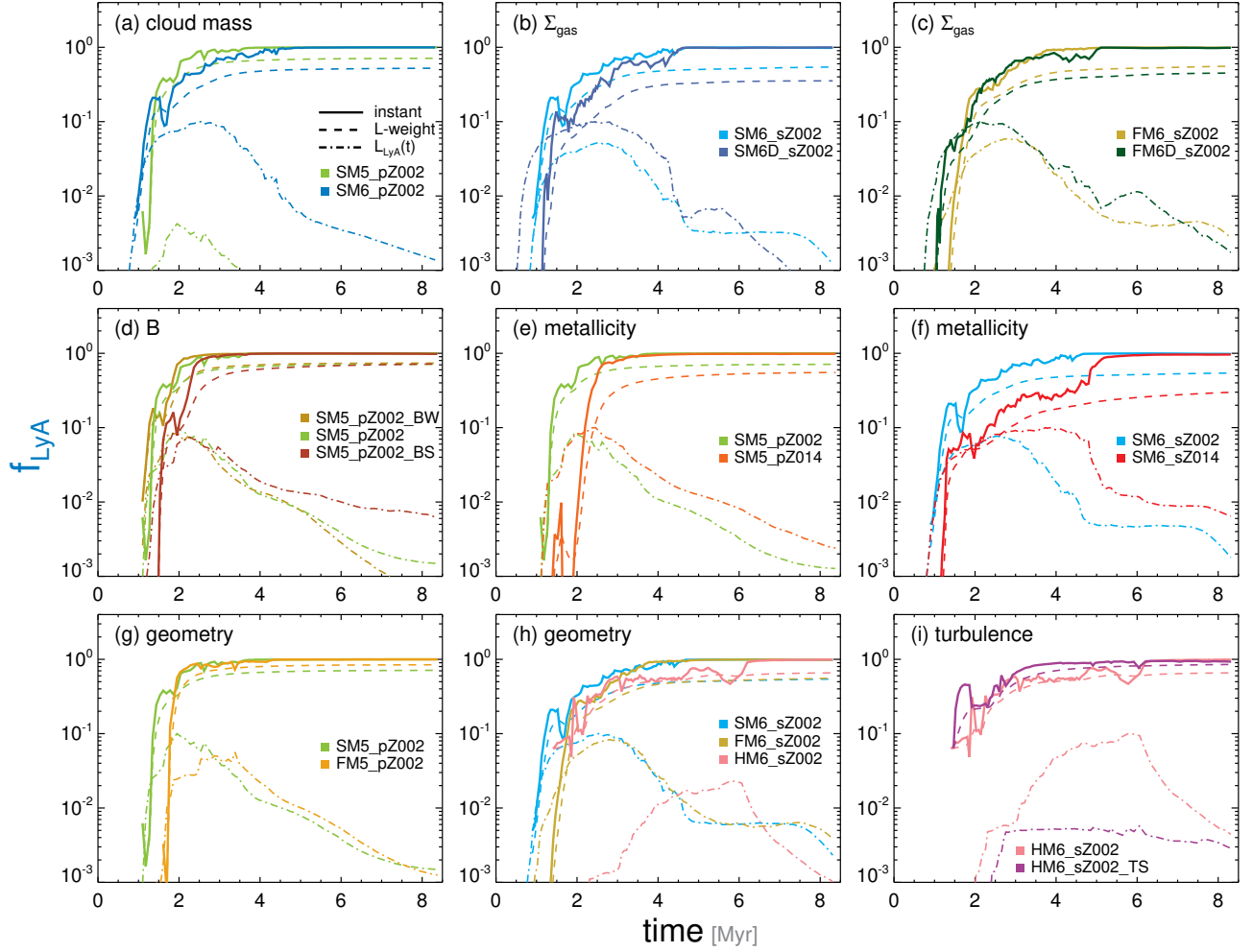


Figure 6. Same as Figure 5, but for Ly α photons. Intrinsic Ly α luminosities are computed from recombinative and collisional processes by taking the gas density and ionized fraction from each computational cell in the simulation. The maximum luminosity is normalized to 0.1 for better readability. Note that Ly α luminosities drop more rapidly than LyC luminosities (Figure 5), since recombinative radiation ($L \propto n_e n_{\text{HII}}$) weakens as the GMCs get dispersed.

is better explained if metal-poor galaxies comprises diffuse GMCs (e.g., $\Sigma_{\text{gas}} = 278 M_{\odot} \text{pc}^{-2}$), or if their typical GMC mass is low (e.g., $10^5 M_{\odot}$).

3.2.3. Metallicity

A comparison of the star formation histories between the metal-poor (Z002) and metal-rich (Z014) runs shows that local dense clumps in our GMCs undergo free-fall collapse and form nearly the same number of stars at $t \lesssim 2.5$ Myr regardless of gas metallicity (Figure 4). In particular, less massive clouds are dispersed on a comparable timescale, and thus the total number of stars formed by the end of the simulation ($t = 8.4$ Myr) is also very similar in the SM5_pZ002 and SM5_pZ014 runs. Yet, a smaller fraction of LyC photons escapes from SM5_pZ014 compared with the metal-poor cloud (57.4% versus 69.0%, Figure 5-(e)). This can be attributed to additional cooling due to metal agents, which mitigates

the effect of photoionization heating and thereby results in a slower propagation of ionization fronts (Kimm et al. 2019; He et al. 2020; Fukushima et al. 2020). In the case of more massive clouds (SM6), fewer stars are formed between $2.5 \lesssim t < 8.4$ Myr in the metal-poor run (SM6_pZ002) as radiation feedback starts to control gas collapse and suppress star formation in the late phases. In spite of the lower SFE $_{\text{tot}}$, the resulting $\langle f_{\text{LyC}} \rangle$ is still significantly higher in metal-poor cases (42.0% versus 34.2%). A similar conclusion was reached in a previous galactic-scale study of LyC escape using idealized disk simulations (Yoo et al. 2020).

The effect of metallicity is somewhat more pronounced in Ly α (Figure 6-(e) and (f)), as $f_{\text{Ly}\alpha}$ emerging from a given structure is higher than f_{LyC} (Dijkstra et al. 2016; Kimm et al. 2019). In the metal-poor GMCs (SM5_pZ002 and SM6_sZ002), $\langle f_{\text{Ly}\alpha} \rangle$ is indeed greater (71.1% and 55.3%) than $\langle f_{\text{LyC}} \rangle$ (69.0% and 42.0%). Interestingly,

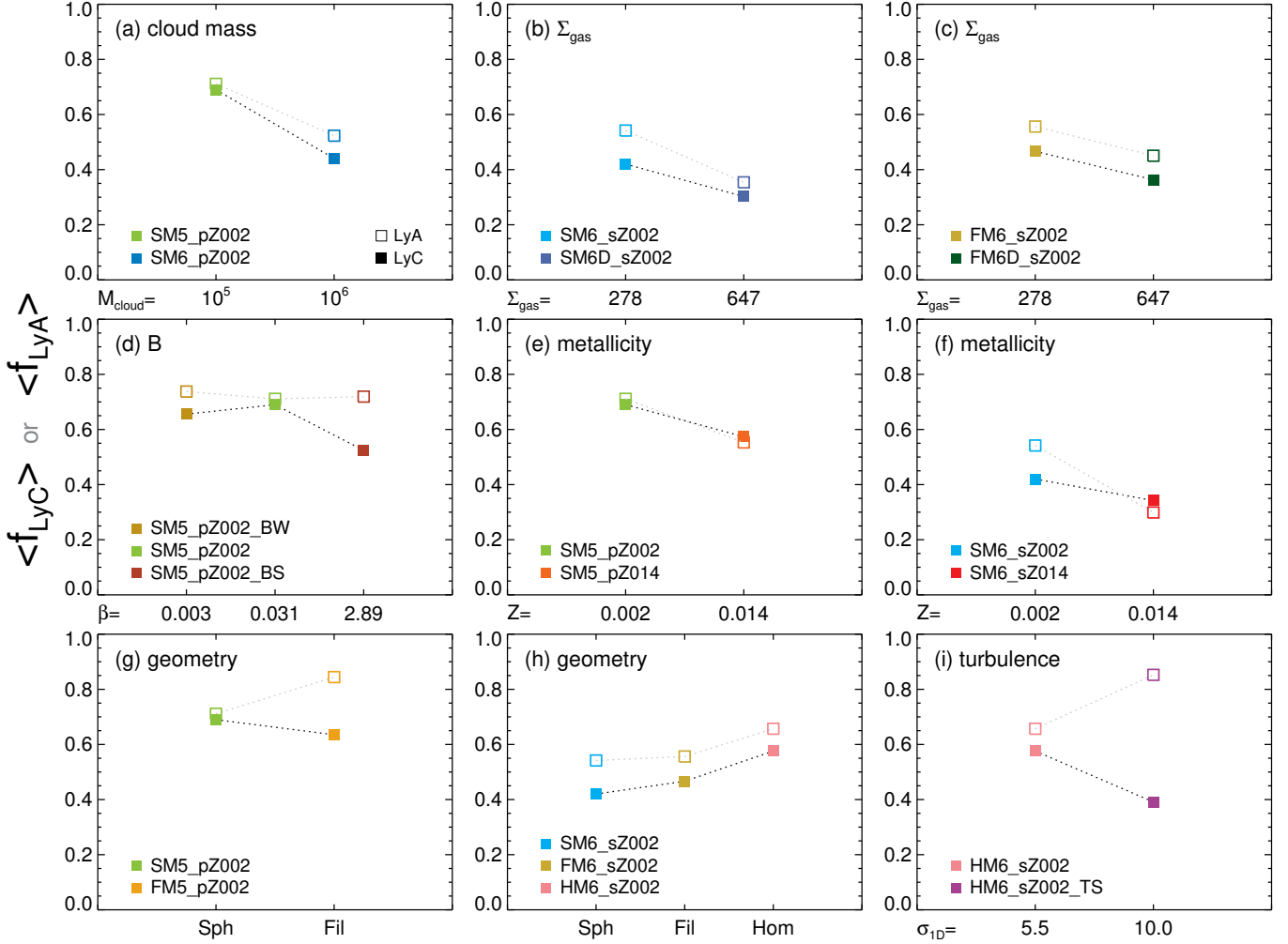


Figure 7. Luminosity-weighted escape fractions of LyC (filled squares) and Ly α photons (empty squares). The escape fractions are averaged over the simulation duration (≈ 8.4 Myr). Different color-codes correspond to runs with various physical properties or resolutions, as indicated in the legend.

the metal-rich GMCs (SM5_pZ014 and SM6_sZ014) exhibit an opposite trend, which can be attributed to different production mechanisms. During LyC dark phases, Ly α photons are generated in the vicinity of young stars, but once the clouds are disrupted and fully ionized, only a few Ly α photons are produced per LyC photon (compare the dot-dashed lines in Figures 5 and 6). At this point, although $f_{\text{Ly}\alpha}$ is close to unity, it does not contribute significantly to the total budget of Ly α photons and hence to the increase in $\langle f_{\text{Ly}\alpha} \rangle$. As a result, $\langle f_{\text{Ly}\alpha} \rangle$ (55.5% and 29.9%) is slightly lower than $\langle f_{\text{LyC}} \rangle$ (57.4% and 34.2%) on GMC scales. However, if we include the contribution from the Ly α photons that are produced by the escaping LyC radiation, $\langle f_{\text{Ly}\alpha} \rangle$ would become larger than $\langle f_{\text{LyC}} \rangle$ on galactic scales.

3.2.4. Magnetic field strength

Figure 5-(c) shows the effect of magnetic fields in the cloud of mass $10^5 M_{\odot}$. We compare three runs (SM5_pZ002_BS, SM5_pZ002, and SM5_pZ002_BW) with different plasma beta parameter ($\beta_P = 0.03, 0.31,$ and 2.89 , respectively), where β_P is ratio of the thermal pressure (P_{th}) to the magnetic pressure (P_{mag}). Note that the mass-weighted magnetic pressure in the fiducial case (SM5_pZ002) is smaller than the turbulent pressure by an order of magnitude, whereas the two pressures are more comparable ($\approx 1:4$) in the strongly magnetized GMC (SM5_pZ002_BS).

In the low- β_P model, gas collapse occurs slowly because of the strong magnetic pressure acting against gravity (e.g., Hennebelle & Iffrig 2014; Girichidis et al. 2018). Star formation is delayed by ≈ 0.3 Myr, and the number of stars formed is the smallest ($\text{SFE}_{\text{tot}} = 0.119$) among the three runs. The escape of ionizing photons is delayed even more significantly (≈ 1 Myr), compared

with the cases with weaker magnetic fields. This is because LyC photons are enshrouded by a larger amount of neutral gas by the time stars are formed and the feedback hence becomes less efficient at breaking out. For example, the luminosity-weighted f_{LyC} of the stars younger than 0.1 Myr in SM5_pZ002 is 5.4%, but in SM5_pZ002_BS it is only 2.5%. We find that part of this difference is already established on small scales; when the escape fraction is measured at 5 pc from each star, $\langle f_{\text{LyC}} \rangle$ is 14.4% and 9.2%, respectively. Although not very significant in terms of photon budget, the escape of LyC photons in the late phase ($t \gtrsim 5$ Myr) is also noticeably reduced in the low- β_P case owing to the combined effects of a lower SFE_{tot} and the higher density of gas remaining in the GMC. Consequently, the neutral fraction of hydrogen increases and a smaller fraction (52%) of LyC photons leaks from their birth cloud (SM5_pZ002_BS) compared with the other runs (66–69%).

Comparison of the runs with weak and fiducial magnetic field strengths reveals a more complex behavior. Until $t \approx 2.5$ Myr, star formation proceeds more efficiently in the run with a weaker B field (SM5_pZ002_BW) than the SM5_pZ002 case. However, this trend is reversed at $t \geq 2.5$ Myr and the SM5_pZ002 run forms more stars since photoionization feedback comes into play earlier than in the other run. Although the differences are not dramatic, the run with a moderate B field forms the largest number of stars and shows the highest escape fraction (69%) among the three cases. Note that this is not the case for the escape of Ly α photons, owing to differences in the Ly α bright phase during cloud evolution.

Our results are consistent with those of RMHD simulations of turbulent clouds performed by Kim et al. (2021b). By simulating five different turbulent seeds per cloud with different magnetic field strengths, the study concluded that strong magnetic fields tend to suppress star formation and the escape fraction. In their study, strongly magnetized clouds with a mass-to-magnetic flux ratio of $\mu_{B,0} = 0.5$ exhibited escape fractions that are twice smaller than those in weakly magnetized cases ($\mu_{B,0} \gtrsim 2$), where $\mu_{B,0} \equiv 2\pi\sqrt{G}\Sigma_{\text{gas}}/B_0$. Similarly, our SM5_pZ002_BS run also yields the smallest $\langle f_{\text{LyC}} \rangle$. However, the difference is less noticeable because the magnetization of our simulated clouds is weaker ($\mu_{B,0} \approx 1.4, 2.3, \text{ and } 14^2$) than the strongest case in Kim et al. (2021b). Moreover, gravitationally, our

simulated clouds are bound better than those of Kim et al. (2021b). The initial virial parameter of the SM5 series is $\alpha_{\text{vir},0} = 5\sigma_{\text{td},0}^2 R_0/GM_0 \approx 1.1$ or 1.4, depending on whether R_0 and M_0 are measured for the inner (10.8 pc) or all (20 pc) layers of the clouds, which is smaller than the value ($\alpha_{\text{vir},0} = 2$) adopted by Kim et al. (2021b). Thus, our simulations are likely to have probed the regime where the effects of magnetic fields are less significant.

3.2.5. Morphology

While previous studies have focused on the escape of LyC and Ly α photons from spherical GMCs, local star-forming clouds often exhibit filamentary structures. Furthermore, GMCs do not necessarily have an isothermal density profile, which is imposed in our spherical cases. Therefore, we examine the effects of morphology on f_{LyC} and $f_{\text{Ly}\alpha}$ in panels (g) and (h) in Figures 5 and 6. Note that filamentary shapes in the FM series are generated using the same initial density distribution employed in the spherical cases (SM series), and thus, any change in the physical properties of star-forming clouds with filamentary structures can be attributed to the morphological difference.

Unlike the spherical case where most of the star particles are formed in the central region, star formation occurs rather slowly along filamentary structures in the FM runs (Figure 8). Owing to the elongated geometry, young stars are less enshrouded by dense gas than in the spherical case, and therefore, they over-pressurize the neighboring region more easily. For example, we find that $3.3 \times 10^5 M_\odot$ of stellar mass is needed to ionize 25% of the total hydrogen in the SM6_sZ002 run, whereas roughly half ($1.8 \times 10^5 M_\odot$) of this stellar mass is needed to achieve the same level of ionization in FM6_sZ002. The resulting SFE_{tot} is decreased from 0.188 (SM5_pZ002) to 0.133 (FM5_pZ002) in the $10^5 M_\odot$ GMCs, and from 0.465 (SM6_sZ002) to 0.319 (FM6_sZ002) in the massive GMCs. Naively, one may think that the filamentary structure would lead to a high escape fraction of ionizing photons, but no clear trend is found in $\langle f_{\text{LyC}} \rangle$ between the two geometries. While the filamentary cloud shows a higher $\langle f_{\text{LyC}} \rangle$ when it is massive, the opposite is true for the less massive cloud. This is likely because a small GMC is more susceptible to photoionization feedback, and because in a spherical cloud, the effects of a higher SFE_{tot} dominate over the geometrical effect that allows for more efficient propagation along low-density channels. On the other hand, $\langle f_{\text{Ly}\alpha} \rangle$ is always larger in filamentary cases, indicating that resonant scattering is more sensitive to the cloud geometry.

² The dimensionless mass-to-magnetic flux ratio is higher in the inner region of the cloud where the isothermal density profile is employed.

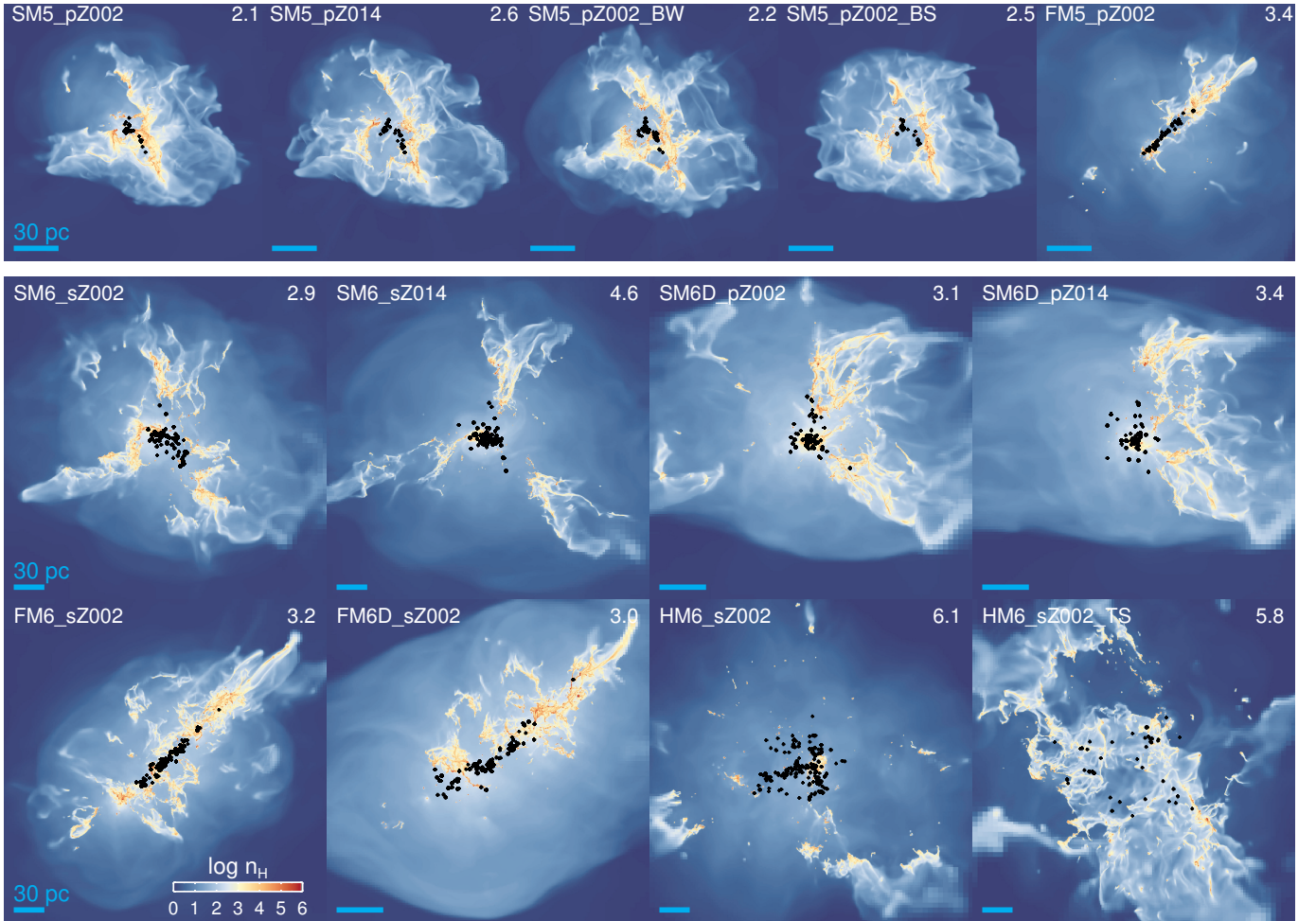


Figure 8. Projected density distributions of GMCs when the escaping Ly α luminosity is the maximum. The time of each snapshot (in Myrs) is specified at the top right corner. Black dots denote stars with $> 8 M_{\odot}$, and the cyan bar measures 30 pc. The simulated clouds show the brightest Ly α emission before they are completely dispersed. An exception is HM6_sZ002, where gas collapses at the center contributes significantly to the total Ly α luminosity.

The most dramatic difference is seen in the run where the gas is homogeneously distributed (HM6_sZ002). Because this homogeneous spherical cloud starts without any central concentration in density, stars are formed late ($t > 2$ Myr), with the peak being around $t = 6$ Myr. SFE_{tot} is also significantly lower (0.174) than the SM6 runs, as photoionization feedback from the early populations effectively controls the gas collapse and star formation in neighboring regions within the GMC. Despite the low SFE_{tot} , their $\langle f_{\text{LyC}} \rangle$ is higher (57.6%) than that of the spherical GMC (SM6_sZ002, 42.0%), as the late-forming stars can take advantage of the low-density channels created by the early generations of stars.

The physical properties of the HM6_sZ002 cloud are similar to those of the M1E6R45 cloud by Kim et al. (2019), and therefore, it is of interest to compare the results for the two runs. Although our virial parameter ($\alpha_{\text{vir},0} = 1.4$) is slightly lower than theirs ($\alpha_{\text{vir},0} = 2$),

the mass and radius are nearly identical and both cases assume a uniform density profile. The resulting SFE_{tot} are comparable (0.174 versus 0.22), despite differences in the numerics and turbulent structures. Kim et al. (2019) found that within the first 3 Myr from the onset of star formation, $\langle f_{\text{LyC}} \rangle$ was 10%, which is very similar to our $\langle f_{\text{LyC}} \rangle$ if the escape fraction is integrated for the first 3 Myr, demonstrating overall consistency.

3.2.6. Turbulence

As demonstrated by Kim et al. (2021b), the presence of strong turbulence regulates star formation and thereby alters the escape of LyC radiation (see also Safarzadeh & Scannapieco 2016; Kakiichi & Gronke 2021). In a similar spirit, we examine the effects of turbulence by imposing a turbulence that is approximately twice ($\sigma_{1d,0} = 10.0 \text{ km s}^{-1}$) stronger than HM6_sZ002. The corresponding virial parameter of the HM6_sZ002_TS run is $\alpha_{\text{vir},0} = 4.6$. Note that we use the homogeneous cloud

to facilitate comparison with other studies and also because its uniform density makes it easier to interpret the impact of turbulence compared with clouds with an isothermal density profile.

Figures 5-(i) and 5-(i) show the impact of turbulence. Because the cloud is no longer gravitationally well bound, star formation proceeds very slowly, and only a small amount of gas is turned into stars. Compared with the HM6_sZ002 run ($\text{SFE}_{\text{tot}} = 0.174$), the total SFE_{tot} is reduced by an order of magnitude in the HM6_sZ002_TS run ($\text{SFE}_{\text{tot}} = 0.013$). However, intriguingly, a significant fraction of LyC photons escapes from the GMC ($\langle f_{\text{LyC}} \rangle = 39.1\%$). This fraction is smaller than that in the weaker turbulence case ($\langle f_{\text{LyC}} \rangle = 57.6\%$), but still substantial and comparable to those for spherical clouds with high SFE_{tot} . The large $\langle f_{\text{LyC}} \rangle$ can be attributed to the extended spatial distribution of young stars that are less enshrouded by the GMC gas compared with stars formed in spherical clouds (Figure 8). An opposite example is the M6_SFE1_sng run from Kimm et al. (2019), where star particles with a mass of 1% of the GMC were placed randomly in the central dense region of $r \lesssim 5$ pc. In this model, only 0.4% of the LyC photons managed to escape from the GMC, which emphasizes the importance of the environment of star forming sites.

Despite the low SFE_{tot} , the escape of Ly α photons is the most efficient in the GMC with strong turbulence. A total of 85.2% of Ly α photons escape from the HM6_sZ002_TS run, while a smaller fraction leaves the homogeneous cloud with weaker turbulence (65.7%). We note that $\langle f_{\text{Ly}\alpha} \rangle$ is even larger than any other clouds with different geometries and high SFE_{tot} . As evident in Figure 6-(i), the Ly α escape fraction is high even before a significant number of stars form and disrupt the cloud ($t \sim 2$ Myr), as the turbulent motions naturally generate low-density channels through which Ly α photons can propagate. Once the LyC radiation permeates the low-density regions, almost all Ly α photons escape from the GMCs, even before SNe explode (see also Kakiichi & Gronke 2021).

3.3. Properties of Ly α spectra

As shown in Figure 3, the shape of Ly α profiles changes dramatically over the lifetime of GMCs. In this subsection, we discuss our investigation of the dependence of Ly α shapes on cloud properties and our qualitative examination of line properties, such as the velocity separation of the double peaks (v_{sep}) and the ratio of the blue part to the red part of the Ly α spectrum ($L_{\text{blue}}/L_{\text{red}}$).

3.3.1. Similar v_{sep} in emergent Ly α

In Figure 9, we present the luminosity-weighted Ly α profiles of the simulated GMCs by stacking the results between the first snapshot that shows star formation and the last snapshot of the simulation that the GMC is mostly dispersed. The Ly α lines show the well-known double-peak profiles, with a more pronounced spectrum redward of Ly α . The asymmetric feature is ubiquitously seen, indicating the presence of neutral outflows resulting from the disruption of clouds. The typical separation of the two velocity peaks is about 90–100 km s^{-1} , and it shows little dependence on the magnetic field strength (panel (d)) or morphology (panels (g) and (h)). On the other hand, GMCs with a higher surface density tend to exhibit a slightly larger $v_{\text{sep}} \approx 120 \text{ km s}^{-1}$, owing to the larger optical depth (panels (b) and (c)). By contrast, more metal-rich runs show a slightly smaller v_{sep} of $\approx 80 \text{ km s}^{-1}$, as Ly α photons are destroyed by dust before too many scattering events occur (panels (e) and (f)).

In order to qualitatively investigate the line features, we compute the location of the red peak by binning the stacked Ly α spectrum with $\Delta v = 2 \text{ km s}^{-1}$ and show it as a function of the relative flux ratio between the blue part and red part of the spectrum ($L_{\text{blue}}/L_{\text{red}}$) in Figure 10. The blue empty circles connected by dotted lines show an example of the time evolution of the metal-poor massive cloud of SM6_sZ002. Note that the earliest stages during which Ly α photons are fully absorbed by dust are not shown. The evolutionary sequence begins around $L_{\text{blue}}/L_{\text{red}} \sim 0.4$ –0.8 when gas outflows start to develop locally. The velocity offset of the red peak is substantial ($v_{\text{peak,red}} \sim 200$ –300 km s^{-1}) in this Ly α -faint phase, but it quickly decreases and settles at $v_{\text{peak,red}} \approx 50 \text{ km s}^{-1}$. This happens mainly because the average column density of the volume-filling neutral hydrogen in later stages of the evolution is maintained around $N_{\text{HI}} \sim 10^{18} \text{ cm}^{-2}$. As mentioned in the literature, the peak of the velocity offset is formed at $v_{\text{peak}} \approx \pm 1.06 (a_V \tau_0)^{1/3} b$ when photons are injected into the center of a homogeneous static slab (Neufeld 1990; Dijkstra et al. 2006; Verhamme et al. 2006), where $a_V = 4.7 \times 10^{-4} T_4^{-1/2}$ is the Voigt parameter, $\tau_0 = \sigma_0 N_{\text{HI}}$ is the optical depth to Ly α at the line center, $T_4 = T/10^4 \text{ K}$ is the temperature in units of 10^4 K , and $\sigma_0 = 5.88 \times 10^{-14} \text{ cm}^2 T_4^{-1/2}$ is the cross-section. Here $b = \sqrt{v_{\text{th}}^2 + \sigma_{\text{turb}}^2}$ is the Doppler parameter, where $v_{\text{th}} = 12.9 \text{ km s}^{-1} T_4^{1/2}$ is the thermal velocity and σ_{turb} is the turbulent velocity. The resulting v_{sep}

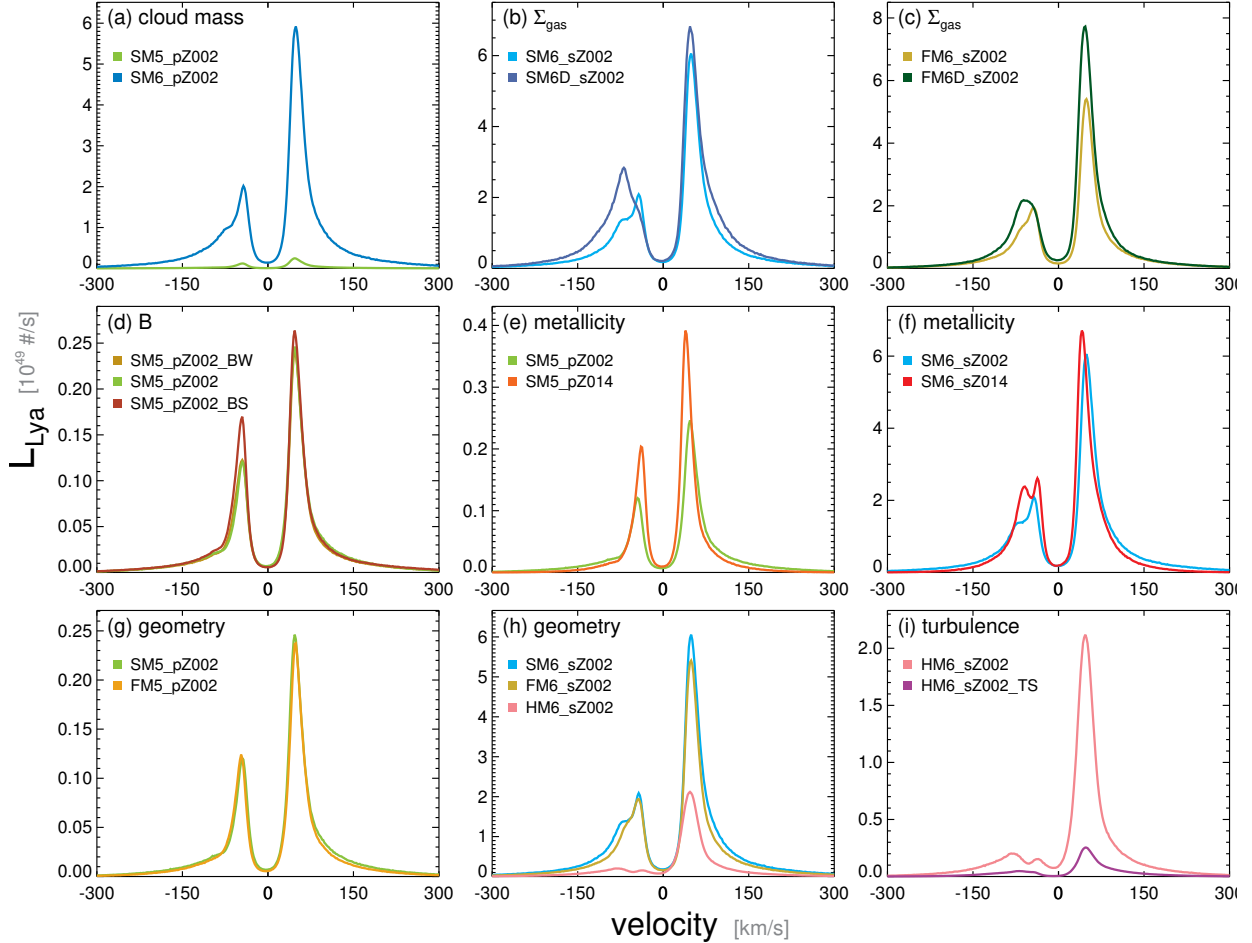


Figure 9. Time-averaged velocity spectra of Ly α photons from simulated GMCs. The abscissa represents the angle-averaged escaping Ly α luminosity summed over each bin in units of 10^{49} #/s, where # is the number of Ly α photons. The bin size is 2 km s^{-1} . Different color-codes correspond to results from simulations with different physical parameters or resolutions, as indicated in the legend.

may be written as

$$v_{\text{sep}} = 82.7 \text{ km s}^{-1} \sqrt{1 + \mathcal{M}^2} \left(\frac{N_{\text{HI}}}{10^{18} \text{ cm}^{-2}} \right)^{1/3} \left(\frac{T}{10^4 \text{ K}} \right)^{1/6} \quad (2)$$

where $\mathcal{M} \equiv \sigma_{\text{turb}}/v_{\text{th}}$ is the turbulent Mach number. Thus, Ly α photons that are scattered in a medium with $T = 20,000 \text{ K}$ and $\sigma_{\text{turb}} \approx 0 - 10 \text{ km s}^{-1}$ would easily produce $v_{\text{peak,red}} \approx 50 \text{ km s}^{-1}$, as evident in Figure 10.

Intriguingly, $v_{\text{peak,red}}$ from the stacked Ly α spectrum (star symbols in Figure 10) is very similar ($v_{\text{peak,red}} \approx 50 \text{ km s}^{-1}$), regardless of the physical properties of the clouds. This is unexpected, given that the average hydrogen column density varies by an order of magnitude from $\langle \log N_{\text{HI}} \rangle \approx 22.3$ in SM5_pZ002 to ≈ 23.2 in SM6D_pZ002. Here, we measure $\langle \log N_{\text{HI}} \rangle$ from the simulation center in the radial direction using the Healpix algorithm along 196,608 sight-lines (Górski et al. 2005). However, the difference in the column density of *neutral* hydrogen is less dramatic as SFE_{tot} tends to be higher

by a factor of 4–5 in the runs with larger $\langle \log N_{\text{HI}} \rangle$ and therefore more ionizing photons are available per unit gas mass.

To corroborate this, we present in Figure 11 example spectra from the SM5_pZ002 and SM6D_pZ002 runs when the largest number of Ly α photons escape from the GMC ($t \approx 3 \text{ Myr}$). The gas distributions at the same epoch are shown in Figure 8. Note that during this Ly α bright phase, there exist dense filaments that continue to form stars, but a large fraction of the GMC is covered with low-density ionized hydrogen. Figure 11 shows that $v_{\text{red,peak}}$ is primarily determined by the cloud gas located within $r \lesssim 30$ (top) or 50 pc (bottom), where the N_{HI} distributions may be characterized by double log-normal profiles with one centered on $\sim 10^{18} \text{ cm}^{-2}$ and the other on $\sim 10^{22} \text{ cm}^{-2}$. The covering fraction of the latter component ($\log N_{\text{HI}} > 19$) is large ($\sim 30\text{--}50\%$) in these snapshots, but insufficient to trap Ly α photons. Thus, Ly α could easily travel away from the dense regions and

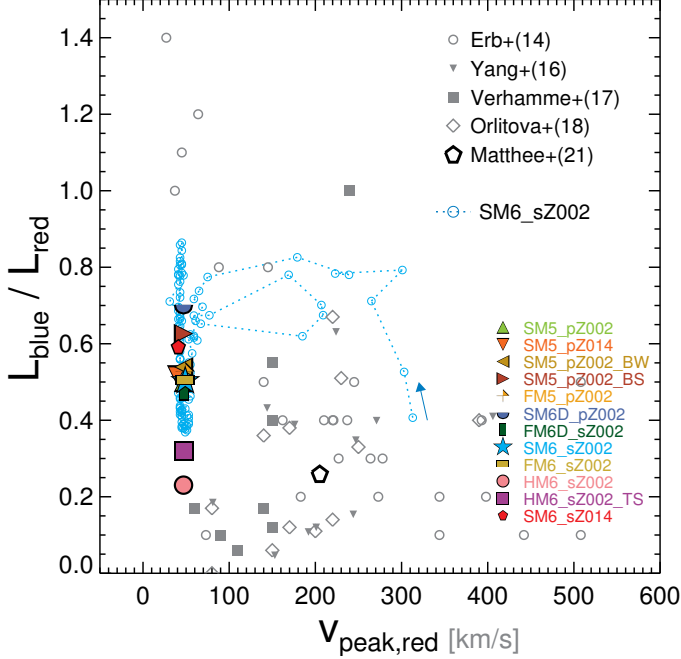


Figure 10. Plot of the location of the red peak ($v_{\text{peak,red}}$) versus the relative flux ratio between the blue part and red part of the Ly α spectrum ($L_{\text{blue}}/L_{\text{red}}$). Blue empty circles connected by dotted lines show an example of the time evolution of a metal-poor massive cloud (SM6_sZ002). Colored symbols indicate values obtained from the stacked Ly α spectrum in each simulation, and observational data are marked in gray color with various symbols, as indicated in the legend.

be scattered in the low density medium at $r \lesssim 30$ or 50 pc, forming the red peak at $\approx 50 \text{ km s}^{-1}$. Likewise, the velocity offset of the blue peak is mostly determined by the gas at $r \lesssim 30$ or 50 pc, but it appears further away from the line center ($v_{\text{peak,blue}} \approx -70\text{--}80 \text{ km s}^{-1}$), similar to the feature associated with zero back-scattering in expanding shells (e.g., Figure 12 in Verhamme et al. 2006). The gas outside the GMC ($r > 30$ or 50 pc) then re-distributes the frequency of any residual photons with $|v| \lesssim 30 \text{ km s}^{-1}$. For example, scattering in the inner region gives rise to a blue peak at $v \approx -80 \text{ km s}^{-1}$ in the SM5_pZ002 run, but more Ly α photons pile up at $v \approx -50 \text{ km s}^{-1}$ after being scattered by the background medium. This effect is not very prominent in the SM6D_Z002 run, as there are fewer Ly α photons close to the line center after the interaction with the GMC. The exact location of the new blue peak found in the SM5_pZ002 run should depend on the assumption about the background ISM, but it is clear from Figure 11 that a similar v_{sep} originates from the scattering with neutral hydrogen in the GMCs.

3.3.2. Flux ratio

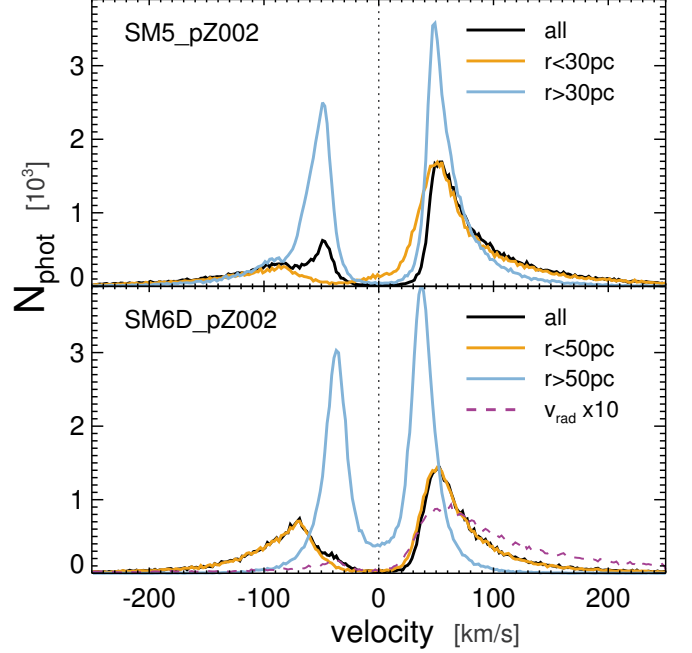


Figure 11. Effects of scattering due to the inner or outer cloud gas in the simulations. The upper panel shows an example of Ly α spectra from the lower-mass metal-poor cloud (SM5_pZ002), while the lower panel exhibits spectra from a massive cloud with high surface density (SM5D_Z002) during the Ly α bright phase (i.e. the same snapshot as in Figure 8). Colored solid lines indicate the spectra in the absence of scattering due to the diffuse ISM region at $r > 30$ or 50 pc (orange) or the dense GMC region at $r < 30$ or 50 pc (blue), where r is the three dimensional radius from the Ly α luminosity center. The black lines correspond to the Ly α spectra processed by the entire gas in the simulated volume. The purple dashed line corresponds to the case in which the radial outflow velocity of the cloud is artificially augmented by a factor of 10.

Figure 10 shows that the typical flux ratio between the blue part and red part of the Ly α profiles is less than unity ($L_{\text{blue}}/L_{\text{red}} \approx 0.4\text{--}0.6$). As shown in Figure 6, simulated clouds are bright in Ly α at $t \sim 2\text{--}4 \text{ Myr}$ during which roughly 50–70% of the initial neutral hydrogen is ionized. Because outflows of the cloud gas are driven by photoionization heating, they are generally slow ($\sim 10 \text{ km s}^{-1}$), and Ly α properties of the simulated clouds occupy a narrower region in the $v_{\text{peak,red}}\text{--}L_{\text{blue}}/L_{\text{red}}$ plane, compared with the observations of actively star-forming galaxies (Erb et al. 2014; Yang et al. 2016; Verhamme et al. 2017; Orlitová et al. 2018).

The relative flux ratio can be further reduced if the outflow velocities are increased. For illustrative purposes, we present a case in which the radial velocity of each outflowing gas cell is artificially augmented by a factor of 10 in the SM6D_pZ002 run (purple dashed line

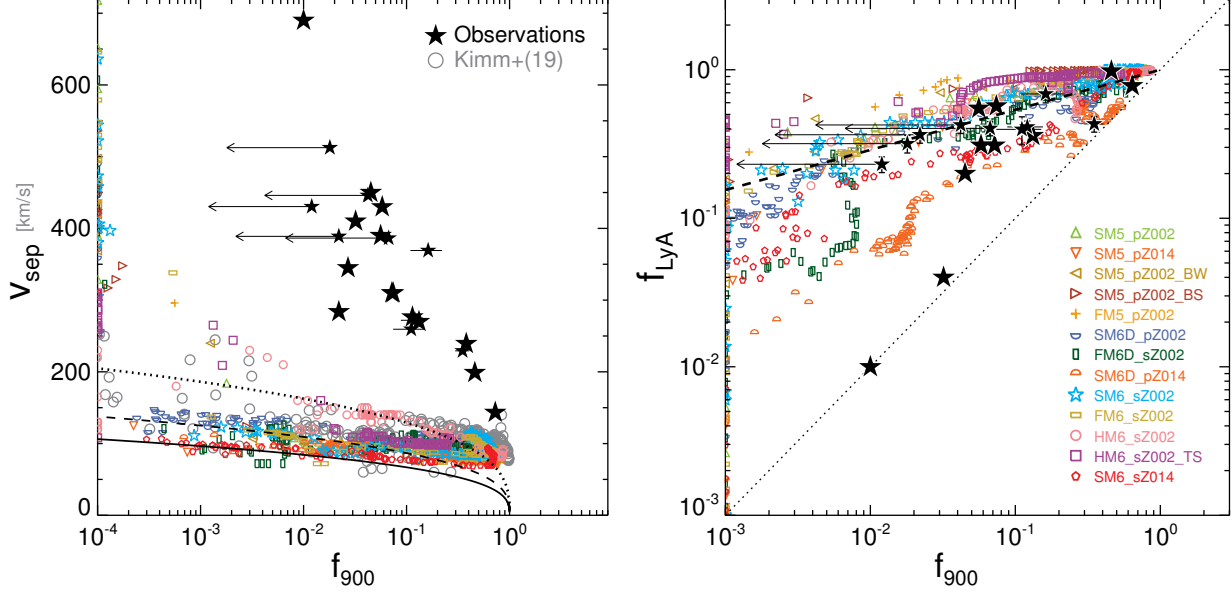


Figure 12. Relationship between the velocity separation of the Ly α double peak (v_{sep}) and the escape fraction at $\lambda \approx 900 \text{ \AA}$ (f_{900} , left panel). Results for our simulated GMCs are shown as colored symbols, as indicated in the legend of the right panel. The gray empty circles indicate earlier results obtained from RHD simulations of GMCs (Kimm et al. 2019). The black star symbols correspond to *galactic-scale* measurements taken from Vanzella et al. (2015); Izotov et al. (2016a,b); Verhamme et al. (2017); Vanzella et al. (2018); Izotov et al. (2018). The smaller star symbol with error bars indicates the results obtained from a low-mass galaxy sample by Izotov et al. (2021). The black lines show simple analytic estimates obtained by assuming $T = 20,000 \text{ K}$ for various turbulent velocities (solid, dashed, and dotted lines: $\sigma = 0, 15,$ and 30 km s^{-1} , respectively). The right panel shows the comparison between f_{900} and $f_{\text{Ly}\alpha}$ on cloud scales. The dashed line indicates a simple fit to our results, $f_{\text{Ly}\alpha} \approx f_{900}^{0.27}$, at $f_{900} > 10^{-3}$.

in Figure 11). Here, the velocity center is chosen as the Ly α luminosity center, and the mass-weighted outflow velocity is increased from 8.2 km s^{-1} to 82 km s^{-1} . We find that the flux ratio is reduced to ≈ 0.15 , stressing the importance of the velocity structure in the formation of $L_{\text{blue}}/L_{\text{red}}$, while the location of the red peak is little changed.

It is also worth noting that optically thick outflows with a large covering fraction can lead to a low flux ratio. By performing a simple Monte Carlo Ly α radiative transfer of a uniform medium with a central source, we confirm that $L_{\text{blue}}/L_{\text{red}} \lesssim 0.1$ if $N_{\text{HI}} = 10^{18} \text{ cm}^{-2}$ and the outflow velocity is 10 km s^{-1} . A more realistic setting of the homogeneous turbulent cloud of HM6_sZ002 also reveals a low $L_{\text{blue}}/L_{\text{red}}$ of ≈ 0.2 , despite the fact that the average outflow velocity of neutral gas is not significant ($\sim 10\text{--}20 \text{ km s}^{-1}$). In the HM6_sZ002 run, $L_{\text{blue}}/L_{\text{red}}$ is kept relatively high ($\gtrsim 0.4$) in the early phase ($t \lesssim 4 \text{ Myr}$), but the slow star formation and SN explosions drive gentle, optically thick outflows that subtend a large solid angle. The flux ratio drops to the minimum of ~ 0.1 at $t > 6 \text{ Myr}$ during which the majority of LyC photons are produced in the HM6_sZ002 run. By contrast, in other spherical or filamentary clouds, strong SN bursts lower the density of the GMC and suppress

Ly α emission at $t \gtrsim 6 \text{ Myr}$. The resulting flux ratio becomes close to unity, as shown as empty blue circles of $L_{\text{blue}}/L_{\text{red}} > 0.6$ in Figure 10. Our numerical experiments thus suggest that simultaneously reproducing the galactic-scale properties of $v_{\text{peak,red}} \sim 100\text{--}200 \text{ km s}^{-1}$ and $L_{\text{blue}}/L_{\text{red}} \sim 0.1\text{--}0.5$ is likely to require optically thick, fast outflows in the ISM/CGM and/or neutral outflows with large covering fractions.

3.3.3. Connection between Ly α and LyC photons

Another common feature of the simulated GMCs is the anti-correlation between the velocity separation and the escape fraction of photons in the wavelength range of $[880\text{ \AA}, 912\text{ \AA}]$ (f_{900}) (Figure 12). This is expected because f_{900} decreases with an increase in N_{HI} , while the number of Ly α scatterings is large in optically thick media. The black lines in Figure 12 exhibit simple analytic estimates obtained from Equation 2 by assuming $T = 20,000 \text{ K}$ for various values of the turbulent velocity (solid, dashed, and dotted lines: $\sigma_{\text{turb}} = 0, 15,$ and 30 km s^{-1} , respectively). Here the analytic f_{900} is approximated as $\exp(-\sigma_{900}N_{\text{HI}})$, where $\sigma_{900} = 6.09 \times 10^{-18} \text{ cm}^{-2}$ is the absorption cross-section at 900 \AA . The simulated clouds are largely consistent with the case with $\sigma_{\text{turb}} = 15 \text{ km s}^{-1}$, which is indeed the typical ve-

locity dispersion of neutral hydrogen in the simulations ($\sigma \sim 10\text{--}15\text{ km s}^{-1}$). There is also a distinctive trend at $f_{900} \gtrsim 0.5$ in the runs of massive clouds, which can be attributed to a strong turbulence ($\sigma \sim 20\text{--}30\text{ km s}^{-1}$) driven by photoionization heating and SN explosions.

Figure 12 further shows that the clouds simulated with different physical conditions follow a similar locus in the $v_{\text{sep}}\text{--}f_{900}$ plane, despite differences in SFE_{tot} . Again, this happens because the neutral column density of the low-density channels through which LyC photons escape is similar ($N_{\text{HI}} \sim 10^{18}\text{ cm}^{-2}$) on GMC scales. As the clouds become ionized and are disrupted, Ly α photons propagate through optically thin, volume-filling gas with $1 \lesssim n_{\text{H}} \lesssim 30\text{ cm}^{-3}$ and a neutral fraction of $10^{-5} \lesssim x_{\text{HI}} \lesssim 10^{-4}$. The low but non-negligible neutral fraction is set by radiation-hydrodynamics calculations, and therefore, v_{sep} of the clouds for a given f_{900} is more sensitive to the disruption phase of the GMCs rather than their initial properties, such as turbulence or metallicity. We also note that the same trend has been observed in RHD simulations of GMCs (Kimm et al. 2019) where massive star particles are placed at random, instead of self-consistently modelling accretion onto sink particles as done in this study, supporting the aforementioned picture.

These findings suggest that the $v_{\text{sep}}\text{--}f_{900}$ sequence is reasonably well defined on GMC scales. Any positive offset from the sequence is likely to indicate the need for additional scattering with neutral hydrogen. Indeed, we find that v_{sep} from simulated GMCs is systematically smaller for a given f_{900} than measured from luminous compact galaxy samples (Vanzella et al. 2015; Izotov et al. 2016a,b; Verhamme et al. 2017; Vanzella et al. 2018; Izotov et al. 2018, 2021). Introducing further scattering by neutral ISM/CGM naturally broadens the Ly α spectra, but the column density should be sufficiently low so that f_{900} is not reduced significantly.

As previously noted, we find that clouds with efficient LyC escape show high $f_{\text{Ly}\alpha}$ (Dijkstra et al. 2016; Kimm et al. 2019, see also Yajima et al. 2014 for galactic scale simulations) (Figure 12, right panel). Although there is substantial scatter, $f_{\text{Ly}\alpha}$ may be approximated as $f_{900}^{0.27}$ in the relatively bright regime ($f_{900} > 10^{-3}$), which is in reasonable agreement with escape fraction measurements of luminous compact galaxies. In principle, LyC photons are significantly absorbed by neutral hydrogen at $N_{\text{HI}} \gtrsim 10^{17}\text{ cm}^{-2}$, while only half of Ly α photons are destroyed by dust even at $N_{\text{HI}} \gtrsim 5 \times 10^{19}\text{ cm}^{-2}$ in the metal-poor ($Z = 0.002$) slab (Neufeld 1990; Hansen & Oh 2006; Verhamme et al. 2006). Therefore, the correlation evident in the right panel of Figure 12 cannot be easily explained by considering different cross-sections of

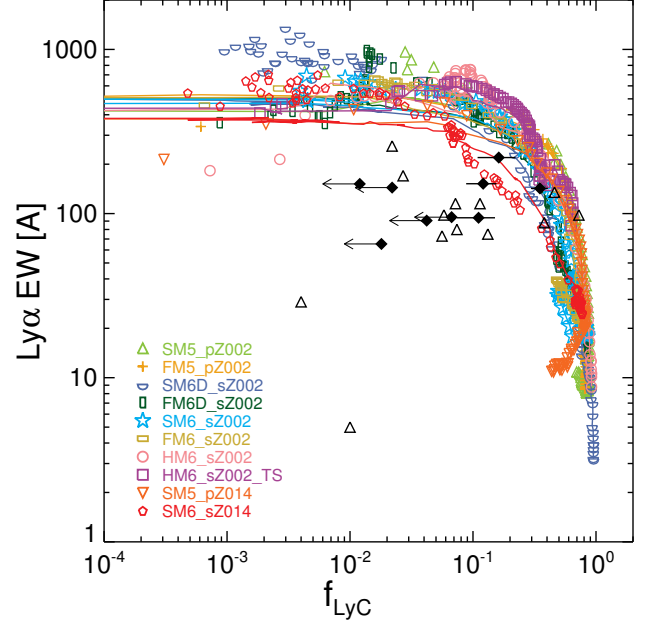


Figure 13. Correlation between the LyC escape fraction and Ly α EW in GMCs. Different symbols show the attenuated Ly α EW in different simulations, as indicated in the legend. The intrinsic Ly α EWs are shown as solid lines, and black empty triangles and filled diamonds represent galactic measurements from Gazagnes et al. (2020) and Izotov et al. (2021), respectively. Note that the attenuated Ly α EWs are often larger than the intrinsic EWs.

LyC and Ly α photons. Rather, it is mainly shaped by the covering fraction of optically thick gas (e.g. Hansen & Oh 2006; Dijkstra et al. 2016). One may wonder whether the correlation is affected by different source positions between Ly α and LyC, but we confirm that the typical densities of the Ly α emitting gas and the host cell of star particles are very similar ($n_{\text{H}} \approx 10^{3\text{--}4}\text{ cm}^{-3}$) during the Ly α bright phase ($t \lesssim 4\text{ Myr}$)³. The question that then arises is how GMCs and galaxies follow similar sequences, despite having marked differences in the N_{HI} distribution. A possible interpretation is that stellar feedback is sufficiently strong to create low-density channels not only in GMCs but also on galactic scales, while high N_{HI} regions are kept shielded, rendering N_{HI} bimodal. Such a bimodal distribution is indeed what we find in our GMC simulations, although the exact locations of the two peaks may differ from those of compact galaxies. Taking one step further, if clouds in compact galaxies share identical physical properties with those

³ At $t \gtrsim 5\text{ Myr}$, Ly α is produced in denser environments ($n_{\text{H}} \sim 5\text{--}10\text{ cm}^{-3}$), compared to LyC ($n_{\text{H}} \sim 0.001\text{--}0.01\text{ cm}^{-3}$), but at this stage not only Ly α but also LyC photons show the escape fractions of unity.

in our simulated GMCs, a higher v_{sep} for the galaxies may be achieved with little effect on f_{900} if the typical column density of the optically thin sight-lines for Ly α ($N_{\text{HI}} \lesssim 10^{18} \text{ cm}^{-2}$) in the compact galaxies is generally increased or if the ISM/CGM is highly turbulent ($1 < \mathcal{M} \lesssim 4$, Equation 2).

Finally, we present the correlation between f_{LyC} and the Ly α equivalent width (EW) in Figure 13. The EW is estimated by comparing the intrinsic or dust-attenuated stellar continuum flux averaged at [1200, 1230]Å from the simple ray tracing (Section 2.3) and the intrinsic or dust-attenuated Ly α luminosities obtained from the RASCAS post-processing (Section 2.2). We find that the intrinsic Ly α EWs are initially very large ($\sim 400\text{--}600 \text{ \AA}$) because of the contribution from hot OB and Wolf-Rayet stars. These EWs are much larger than those of young stellar populations (Charlot & Fall 1993) or those observed in actively star-forming galaxies at high redshift (e.g., Malhotra & Rhoads 2002; Santos et al. 2020), but quickly drop to $\sim 100 \text{ \AA}$ around 3 Myr from the onset of star formation. In the Ly α bright phase ($t \lesssim 3 \text{ Myr}$), f_{LyC} varies from $< 10^{-4}$ to ~ 0.1 , resulting in the flat sequence for $f_{\text{LyC}} \lesssim 0.1$. Once the GMCs are sufficiently dispersed, Ly α EWs decrease to about 10 \AA , while f_{LyC} keeps increasing at $\gtrsim 0.1$; thus, there exists a negative correlation between f_{LyC} and Ly α EW on GMC scales. Dust absorption tends to be more significant for the continuum photons than Ly α during LyC faint phases, leading to extreme Ly α EWs of up to $\sim 1000 \text{ \AA}$. The trend found in our GMC simulations is evidently distinct from that of the LyC leaker data at $0.2 \lesssim z \lesssim 0.4$ (Gazagnes et al. 2020; Izotov et al. 2021), but the absorption associated with the ISM/CGM and/or the presence of an underlying stellar population should easily alleviate the difference between our GMC results and galactic measurements (Song et al. *in prep*).

4. DISCUSSION

Having acquired an understanding of the detailed properties of escaping LyC and Ly α photons, we now discuss the correlation between $\langle f_{\text{LyC}} \rangle$ and or destruction timescale of the GMC (τ_{dest}). We also discuss a possible way to infer f_{LyC} from photons with different wavelengths. The limitations and caveats of this study are also presented later in this section.

4.1. Correlation between $\langle f_{\text{esc}} \rangle$ - SFE_{tot}

An interesting conclusion of Kimm et al. (2017) is that the escape of LyC photons is more efficient if the gas mass enshrouding young stars is smaller (see their Figure 13). Using sub-pc resolution, cosmological RHD simulations of atomic-cooling halos with a mass of $\sim 10^8 M_{\odot}$,

they measured the escape fraction for individual star formation events and demonstrated that it correlates well with the ratio between the amount of dense gas that cannot be photoionized and the photon production rate. This suggests that for a given gas mass, a more efficient star formation episode would lead to a higher f_{LyC} . The results of Kimm et al. (2019) also support this picture in that a larger fraction of LyC photons escapes from GMCs with an SFE_{tot} of 10% compared with those with a SFE_{tot} of 1%.

To further investigate this idea, we plot SFE_{tot} against $\langle f_{\text{LyC}} \rangle$ in Figure 14. GMCs with different morphologies are indicated by different symbols, and clouds with a smaller mass ($10^5 M_{\odot}$) are shown as smaller triangles. We also re-measure luminosity-weighted escape fractions until $t = 10 \text{ Myr}$ for the $10^6 M_{\odot}$ clouds of Kimm et al. (2019). In marked contrast to the previous results obtained from GMCs with SFE_{tot} of $\leq 10\%$ (Kimm et al. 2019), we find that in the current simulations the escape fraction is anti-correlated with SFE_{tot} in actively star-forming GMCs ($20\% \lesssim \text{SFE}_{\text{tot}} \lesssim 80\%$). Clouds with high surface densities convert the majority of the gas into stars, but their $\langle f_{\text{LyC}} \rangle$ is found to be the lowest. This can be attributed to the fact that massive stars are obscured by optically thick media, which are difficult to photoionize owing to their high density for a given ionizing emissivity. While the offset between the time at which the ionizing luminosity reaches 50% of its maximum and the time at which f_{LyC} becomes 50% is $\approx 2 \text{ Myr}$ for SM6_sZ002, the offset is longer ($\approx 3 \text{ Myr}$) in a run with a higher SFE_{tot} (SM6D_sZ002) (see also panel (b) from Figure 5). The difference in the offset is modest ($\approx 1 \text{ Myr}$), but as the majority of ionizing photons are produced in the first $t \lesssim 5 \text{ Myr}$, the resulting $\langle f_{\text{LyC}} \rangle$ differs by a factor of 2 ($\sim 40\%$ versus 20%).

In the other regime where turbulence prevents the cloud from collapsing beyond $\approx 1\%$ (HM6_sZ002_TS), $\langle f_{\text{LyC}} \rangle$ is again reduced to $\approx 40\%$, compared with $\langle f_{\text{LyC}} \rangle \approx 60\text{--}70\%$ from the less massive M5 clouds. The decrease is largely due to the finite number of LyC photons from massive stars and thus the slower propagation of ionization fronts. Kimm et al. (2019) also pointed out that $10^6 M_{\odot}$ clouds with SFE_{tot} of 1% exhibit a small $\langle f_{\text{LyC}} \rangle$ of $\sim 1\text{--}5\%$ when the star particles are randomly placed at $r \lesssim 5 \text{ pc}$ from the cloud center. In our case, a larger $\langle f_{\text{LyC}} \rangle$ of $\approx 40\%$ is obtained in the HM6_sZ002_TS run because strong turbulence allows LyC radiation to escape through a porous medium. However, the escape fraction may be reduced if the propagation of ionization fronts is delayed because of a low SFE_{tot} caused by non-thermal pressure, such as strong magnetization. Simulations of low-mass ($10^5 M_{\odot}$), magnetized GMCs per-

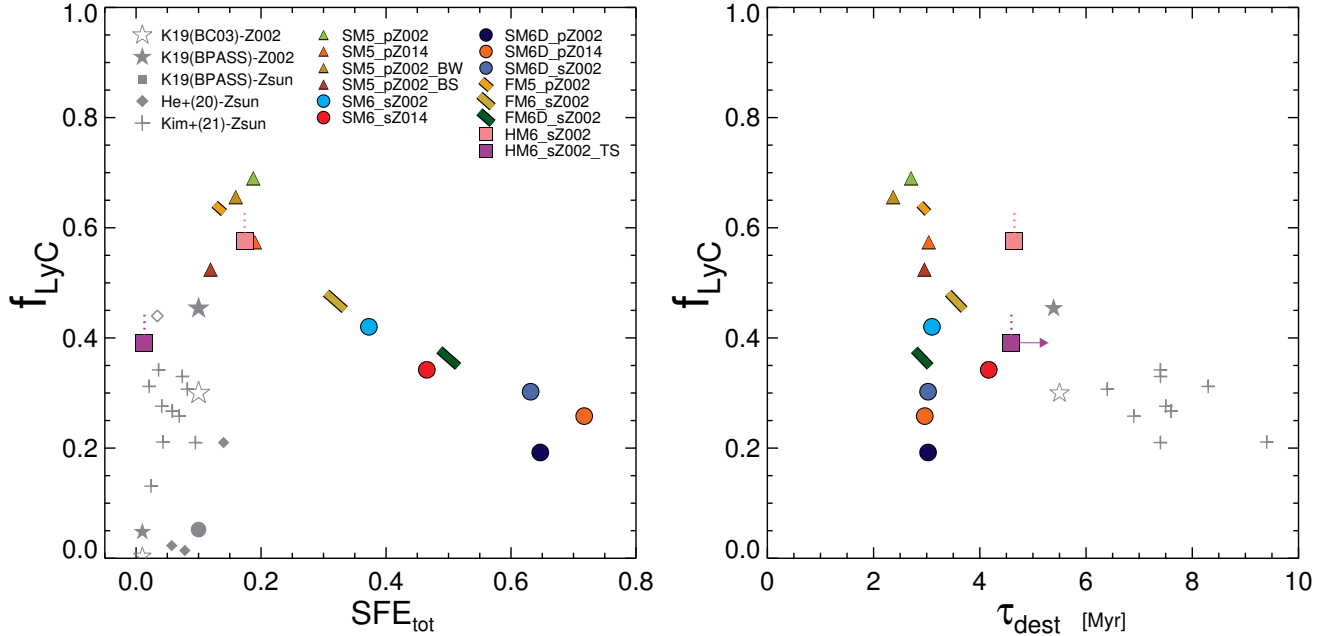


Figure 14. Correlation between the luminosity-weighted escape fraction and the total star formation efficiency in the simulated clouds (left). Different symbols indicate the results from the runs with different simulation parameters, as indicated in the legend. Clouds with a smaller mass ($10^5 M_\odot$) are shown with smaller symbols. Dotted lines correspond to the extrapolated luminosity-weighted escape fraction measured until $t = 20$ Myr assuming that f_{LyC} is kept the same as the value in the final snapshot. Also included as grey star symbols are the escape fractions from Kimm et al. (2019) with the single (empty) or binary stellar evolution model (filled). Bigger star symbols indicate the results measured from $10^6 M_\odot$ clouds, while the small star symbols correspond to those from $10^5 M_\odot$ clouds. The grey filled square shows the solar metallicity case from Kimm et al. (2019). Grey crosses display $\langle f_{\text{LyC}} \rangle$ measured from 10^5 clouds by Kim et al. (2021b). The simulated data for clouds with $10^5 \leq M_{\text{cloud}} \leq 3 \times 10^5 M_\odot$ from He et al. (2020) are shown as filled grey diamonds. Note that there is a clear correlation between SFE_{tot} and the luminosity-weighted escape fraction of LyC photons. The right panel indicates the correlation between the escape fraction and the destruction timescale of dense gas (τ_{dest}). We define τ_{dest} as the time between the onset of star formation and the moment at which the amount of gas with $n_{\text{H}} \geq 100 \text{ cm}^{-3}$ drops to $0.1 M_{\text{cloud}}$.

formed by Kim et al. (2021b) indeed show that $\langle f_{\text{LyC}} \rangle$ is reduced from 30% in their runs with $\mu_{\text{B},0} = \infty$ where SFE_{tot} is 0.08 to 13% in the $\mu_{\text{B},0} = 0.5$ runs where SFE_{tot} is 0.02. Taken together, we are thus led to conclude that $\langle f_{\text{LyC}} \rangle$ is likely to be maximal at intermediate SFE_{tot} (~ 0.2) in GMCs with 10^5 – $10^6 M_\odot$ ⁴.

The relation between SFE_{tot} and $\langle f_{\text{LyC}} \rangle$ shows that these quantities both result from the same evolutionary process of the clouds. As can be seen in Figure 14, the main drivers of this mechanism are the initial surface density and the level of turbulence (or virial parameter), which are modulated to second order by the shape, magnetic field strength, and metallicity of the gas.

4.2. Correlation between $\langle f_{\text{esc}} \rangle$ – τ_{dest}

Because the escape of LyC radiation depends on the evolution of the GMC, it is reasonable to conjecture that $\langle f_{\text{LyC}} \rangle$ may be characterized by the destruction timescale of the GMCs. In Figure 14 (right panel), we show τ_{dest} , the time between the onset of star formation and the moment at which the mass of the dense gas with $n_{\text{H}} \geq 100 \text{ cm}^{-3}$ falls below 10% of its initial value⁵. The figure demonstrates that in the current simulations the correlation between τ_{dest} and $\langle f_{\text{LyC}} \rangle$ is rather weak. Although the low-mass GMCs having the maximal $\langle f_{\text{LyC}} \rangle$ can be explained by the rapid disruption of the clouds, there is non-negligible scatter in the diagram because the destruction of the dense (molecular) gas does not necessarily mean that the GMC is entirely transparent

⁴ He et al. (2020) performed RMHD simulations of GMCs with 3×10^3 – $3 \times 10^5 M_\odot$, and found that $\langle f_{\text{LyC}} \rangle$ decreases with increasing SFE_{tot} . This potentially suggests that the dependence of $\langle f_{\text{LyC}} \rangle$ on SFE_{tot} may be different in lower-mass clouds with $M_{\text{cloud}} < 10^5 M_\odot$.

⁵ We choose this definition to facilitate a comparison with other studies. On the basis of the RHD simulations of Kimm et al. (2019), we measured the timescale at which 95% of molecular hydrogen is dissociated (Kim et al. 2021b) and found that this roughly matches the timescale at which 90% of the dense gas with $n_{\text{H}} \geq 100 \text{ cm}^{-3}$ is destroyed.

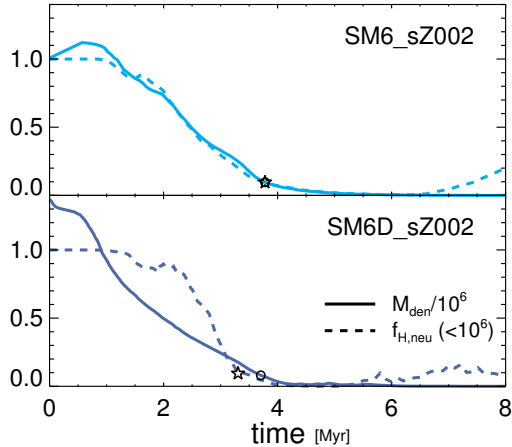


Figure 15. Differences in the development of ionized bubbles in GMCs with normal (upper panel) and high gas surface density (lower panel). The solid lines indicate the amount of dense gas with $n_{\text{H}} \geq 100 \text{ cm}^{-3}$, divided by $10^6 M_{\odot}$. The dashed lines show the neutral fraction of hydrogen within a radius inside which the total gas mass is $10^6 M_{\odot}$. The circle and star symbols correspond to the moment at which the fraction of dense gas and the fraction of neutral hydrogen fall below 0.1, respectively. Note that the destruction timescales are similar for the two GMCs, but a larger portion of the gas is kept neutral for an extended period of time in the run with higher gas surface density (compare the dashed lines at 2–3 Myr).

to LyC. For this to happen, the column density should drop below $N_{\text{HI}} \sim 10^{17} \text{ cm}^{-2}$.

To single out the origin of the difference in $\langle f_{\text{LyC}} \rangle$ for clouds with similar τ_{dest} , we plot in Figure 15 the amount of the dense gas with $n_{\text{H}} \geq 100 \text{ cm}^{-3}$ divided by $10^6 M_{\odot}$, and the neutral fraction of the central $10^6 M_{\odot}$ gas in the two runs (SM6_sZ002 and SM6D_sZ002) whose τ_{dest} are similar (3.1 and 3.5 Myr, respectively). The initial dense gas mass in the SM6_sZ002 cloud is $10^6 M_{\odot}$, but it increases slightly as the gas in the outer envelope with $n_{\text{H}} = 50 \text{ cm}^{-3}$ collapses. On the other hand, the outer envelope gas is considered as a dense component in the SM6D_sZ002 case because of its high initial density ($n_{\text{H}} = 176 \text{ cm}^{-3}$), and the solid line in the bottom panel starts at $\approx 1.4 \times 10^6 M_{\odot}$. Note that stars begin to form earlier ($\Delta t \approx 0.5 \text{ Myr}$) in the dense cloud than in the fiducial run (Figure 4), and therefore the neutral fraction should drop first in the dense cloud if ionization fronts propagate at a similar speed. Yet, we find that while the dense component is efficiently dispersed in the SM6D_sZ002 run, the ionized bubble develops slowly, and a large fraction of the central $10^6 M_{\odot}$ gas is maintained neutral for an extended period of time, unlike the fiducial surface density run (SM6_sZ002). Therefore, apart from the destruction timescale for the dense gas, the

ionization speed also matters for setting up $\langle f_{\text{LyC}} \rangle$ on cloud scales.

We also note that the correlation between $\langle f_{\text{LyC}} \rangle$ and τ_{dest} may be more evident if the results from the clouds with different surface densities are included in Figure 14. Kim et al. (2021b) found that the destruction timescales for $10^5 M_{\odot}$ clouds with a lower Σ_{gas} are longer ($\tau_{\text{dest}} \sim 6 - 10 \text{ Myr}$) than those of our low-mass GMCs, while their $\langle f_{\text{LyC}} \rangle$ tends to be smaller. Because the gas collapse and star formation occurs slowly, the clouds are disrupted on longer timescales, and LyC photons emitted from the stars formed early are easily absorbed. In this regard, τ_{dest} may be seen as a rough indicator of $\langle f_{\text{LyC}} \rangle$, but more simulations are needed to validate the connection between $\langle f_{\text{LyC}} \rangle$ and τ_{dest} based on the same numerical framework.

4.3. Inferring f_{esc} from Ly α , UV, and H α

In observations, constraining the escape of LyC photons from high- z galaxies is a difficult task because the ionizing flux is usually very faint owing to significant attenuation by the neutral ISM and the IGM. Alternative methods based on [CII] $158 \mu\text{m}$ and [OIII] $88 \mu\text{m}$ emission lines (Katz et al. 2020), or UV absorption lines such as CII 1334 \AA (Mauerhofer et al. 2021), Si II 1260 \AA (Gazagnes et al. 2018), or Ly α (Verhamme et al. 2015), have thus been proposed. In a similar spirit, we compare f_{LyC} with the escape fraction of photons at different wavelengths and examine if other often-used emission lines may be used to infer f_{LyC} .

In Figure 16, we present the luminosity and escape fraction of photons in UV and optical bands. The UV luminosity at 1500 \AA is computed by integrating the flux at $[1475, 1525] \text{ \AA}$, and we apply SMC-type or MW-type dust attenuation for the clouds with $Z = 0.002$ or $Z = 0.014$, respectively, based on Weingartner & Draine (2001). The emissivity of the Balmer α line at 6562.8 \AA is calculated as,

$$\varepsilon_{\text{rec,H}\alpha} = n_e n_p P_{\text{B,H}\alpha}(T) \alpha_B(T) e_{\text{H}\alpha}, \quad (3)$$

where n_e and n_p are the number densities of electrons and protons, respectively, $P_{\text{B,H}\alpha}$ is the probability for a recombination event to produce a H α photon (Storey & Hummer 1995), $\alpha_B(T)$ is the temperature-dependent Case B recombination coefficient (Hui & Gnedin 1997), and $e_{\text{H}\alpha} = 1.89 \text{ eV}$ is the energy of the photon. As is the case for Ly α photons, we randomly choose the initial frequency of the H α photons using a Gaussian distribution with the thermal Doppler broadening for individual cells. We also calculate L_{900} by integrating the flux between $[880, 910] \text{ \AA}$.

Figure 16 shows that Ly α is the most luminous among the four observables (L_{900} , $L_{\text{Ly}\alpha}$, L_{1500} , $L_{\text{H}\alpha}$) in the

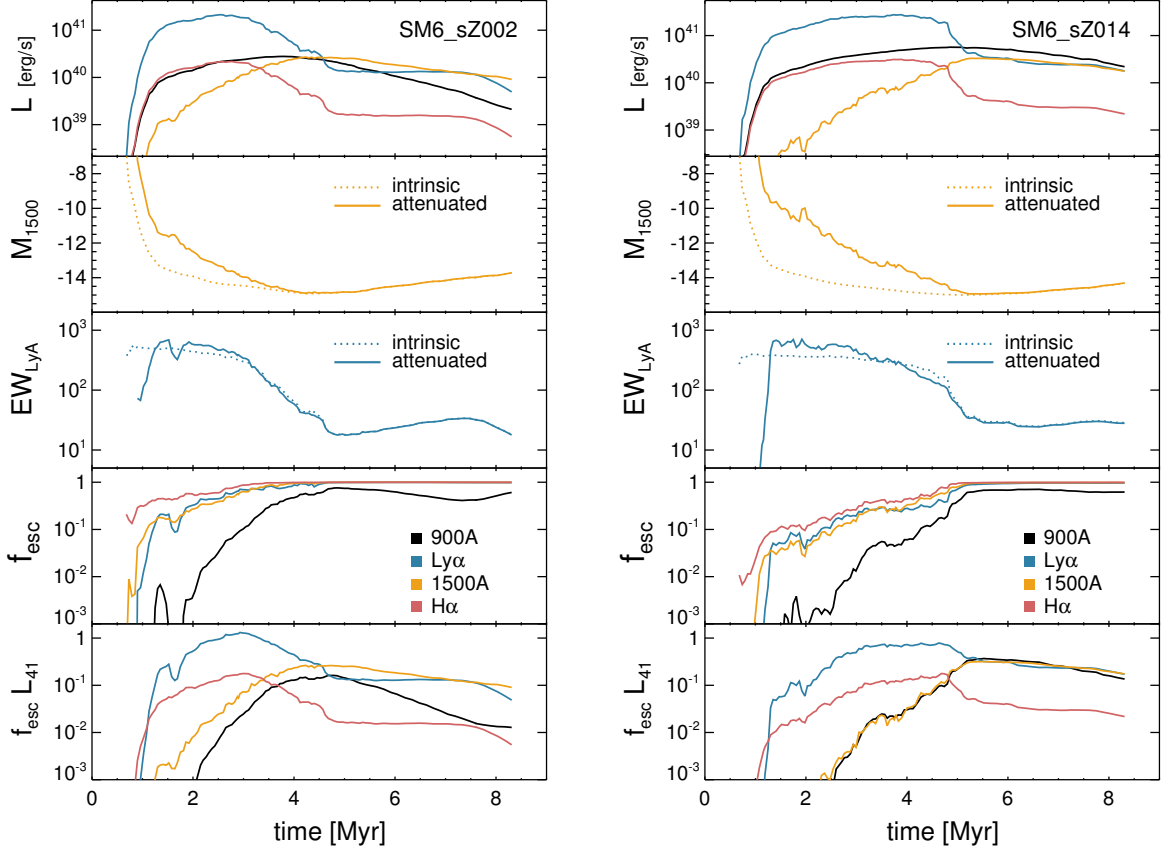


Figure 16. The intrinsic luminosities and escape fractions of photons with various wavelengths from the metal-poor (SM6_sZ002; left) and metal-rich cloud (SM6_sZ014; right). From top to bottom, each row indicates the intrinsic luminosity in units of ergs^{-1} , UV magnitude at 1500 Å, Ly α equivalent width in Å, escape fraction, and escaping luminosity, normalized to 10^{41}ergs^{-1} . Photons with different wavelengths are shown as different colors.

early phase ($t \lesssim 4 \text{Myr}$) of the GMC evolution. $L_{\text{Ly}\alpha}$ becomes comparable to the luminosities at 900 and 1500 Å later, as LyC photons escape efficiently from the clouds and the recombination process becomes inefficient. H α luminosities share the same trend as $L_{\text{Ly}\alpha}$, but are smaller by a factor of 8–10 because of the difference in the photon energy and the transition probability. The Ly α EWs are initially quite high ($\sim 500 \text{Å}$), but decreases to a few tens of Å. Recombination lines (Ly α and H α), including LyC radiation, emerge very quickly as star formation proceeds, but the flux at 1500 Å develops rather slowly. This can be attributed to massive stars in the zero age main sequence becoming more luminous in the early phase of hydrogen burning, as nuclear reactions are enhanced due to the temperature increase in the convective stellar core (e.g. [Iben 1967](#)). The UV light from the simulated clusters is affected by significant dust attenuation ($A_{1500} \lesssim 2\text{--}4$) until the clouds are dispersed, and it then reaches the maximum luminosity of $M_{1500} \approx -15$ in AB magnitude. Such clusters are challenging to detect at the epoch of reionization even with the Hubble Space Telescope imaging (e.g., [Liver-](#)

[more et al. 2017; Atek et al. 2018](#)), but may be accessible with the James Webb Space Telescope or deep MUSE observations of Ly α emission via strong lensing (e.g., [Vanzella et al. 2020](#)).

The escape fractions of Ly α and the UV photons at 1500 Å appear to trace each other reasonably well (Figure 16). This is essentially because of the clumpy gas distributions that simultaneously block both photons along some sight-lines ([Hansen & Oh 2006](#)), not because of the similar dust absorption cross-sections. The resonant nature of Ly α increases the interaction probability with dust, and approximately half of the Ly α photons are destroyed at $N_{\text{HI}} \approx 5 \times 10^{19} \text{cm}^{-2}$ in the case of SMC-type dust with $Z = 0.002$, assuming a uniform medium of $T = 10^4 \text{K}$ (e.g., [Verhamme et al. 2006](#)). By contrast, despite the proximity in wavelength, the UV photon in 1500Å requires ≈ 40 times higher N_{HI} to be absorbed by dust. This is more clearly illustrated in Figure 17 (bottom left panel), where we present the escape fraction measurements of simulated GMCs along with simple analytic estimates of the escape fraction in a uniform medium. While only 0.1% of Ly α photons

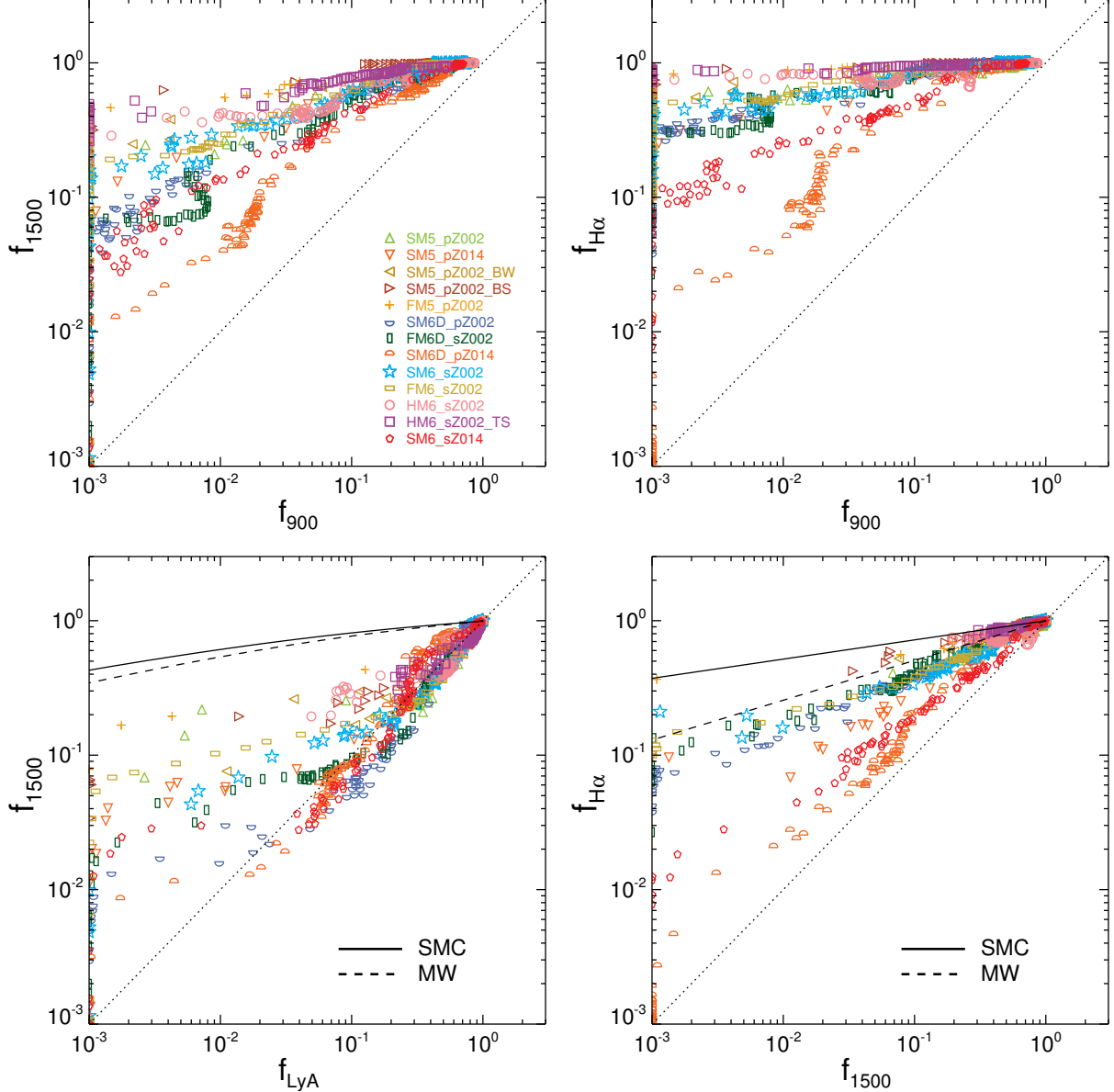


Figure 17. The correlation between the escape fraction of various wavelengths. The colored symbols show simulated escape fractions measured at different times from GMCs with different conditions, as indicated in the legend. The dotted line shows one-to-one correspondence. The solid and dashed lines in the bottom panels exhibit the correlation predicted from the uniform media with Small Magellanic Cloud-type or Milky Way-type dust. Note that the simulated GMCs display a steeper correlation than the uniform case, indicating that the UV photons are absorbed by clumpy gas distributions.

would survive in a uniform medium regardless of the dust model assumed, a significant fraction ($\approx 40\%$) of the UV photons would be transmitted according to the simple analytic model. However, the simulated GMCs show similar f_{1500} and $f_{\text{Ly}\alpha}$ for $f_{\text{Ly}\alpha} \gtrsim 0.1$, although f_{1500} becomes systemically larger for $f_{\text{Ly}\alpha} \lesssim 0.1$, as N_{HI} distributions in the early clouds are not as clumpy as those at the late phase of the GMC evolution.

Our results thus suggest that the escape fraction at 1500 \AA can only be as useful as $\text{Ly}\alpha$ in selecting poten-

tial LyC leakers. It is indeed evident from Figure 17 (top left panel) that not only $f_{\text{Ly}\alpha}$ but also f_{1500} is systematically higher than $f_{\text{Ly}\alpha}$, with dusty clouds being less efficient in leaking UV photons. Nevertheless, the extreme UV condition $f_{1500} \gtrsim 0.5$ is likely to increase the probability of finding GMCs with $f_{900} \gtrsim 0.1$, compared with a blind survey. The post-processing of a cosmological SPH simulation run with lower resolutions ($250 h^{-1} \text{ pc}$ and $3 \times 10^5 h^{-1} M_{\odot}$) also showed that the UV con-

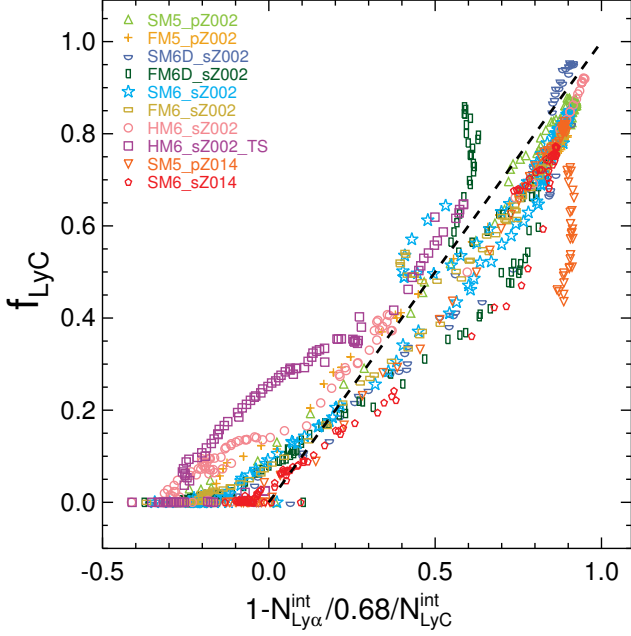


Figure 18. Escape fraction of LyC radiation deduced from the number of Ly α photons produced per second ($f'_{\text{LyC}} \equiv 1 - \dot{N}_{\text{Ly}\alpha}^{\text{int}}/0.68/\dot{N}_{\text{LyC}}^{\text{int}}$). The runs with different input parameters are shown as different symbols and color-codings, as indicated in the legend. For comparison, we display a one-to-one relation as a dashed line. The inferred escape fractions (f'_{LyC}) reasonably match the true f_{LyC} in the range $f'_{\text{LyC}} \gtrsim 0.1$, albeit with significant scatter ($\Delta f_{\text{LyC}} \sim 0.2$). Note that f'_{LyC} tends to be greater than f_{LyC} at $f'_{\text{LyC}} \gtrsim 0.4$ (see the text).

dition may be used to find LyC leakers even on galactic scales (Yajima et al. 2014).

Compared with UV or Ly α photons, H α photons are less affected by dust, and they escape more efficiently from the GMC (top right panel). Except for the metal-rich massive cloud (SM6_sZ014), the majority of simulated data show $f_{\text{H}\alpha} \gtrsim 0.5$, making $f_{\text{H}\alpha}$ the least favored indicator for selecting potential LyC leakers. The bottom right panel in Figure 17 shows that there is a positive correlation between $f_{\text{H}\alpha}$ and f_{1500} , but again, $f_{\text{H}\alpha}$ is smaller than the simple estimate obtained from attenuation due to a uniform SMC or MW-type dust, indicating the effect of the clumpy gas distribution. The simulated clouds also show a more significant deviation from the analytic estimates (solid or dashed lines) in the $f_{\text{Ly}\alpha}$ – f_{1500} plane than in the $f_{\text{H}\alpha}$ – f_{1500} plane. This implies that the typical column density of the clumpy gas is not significantly higher than $N_{\text{H}} \sim 10^{22} \text{ cm}^{-2}$, given that the dust absorption cross-section at 1500 Å is only 7 (3.4) times that at 6563 Å in the case of the SMC-type (MW-type) dust.

Although the use of escape fractions may not be practical to directly infer f_{LyC} , Ly α (or H α) luminosities may be a promising alternative. If the majority of Ly α photons are produced by recombinative radiation, the number of Ly α photons produced per second ($\dot{N}_{\text{Ly}\alpha, \text{int}}$) can be approximated as $\dot{N}_{\text{Ly}\alpha, \text{int}} \approx P_B(T) \dot{N}_{\text{LyC}, \text{abs}}$, where $\dot{N}_{\text{LyC}, \text{abs}}$ is the number of LyC photons absorbed per second and $P_B(T)$ is the temperature-dependent transition probability. In a completely ionized medium with $T = 10^4 \text{ K}$, $P_B(T)$ is 0.68. Collisional radiation adds to the total Ly α luminosity, and we find that its fractional contribution is less than $\approx 30\%$, consistent with Kimm et al. (2019, see their Figure 8). Neglecting collisional radiation, the escape fraction can be approximately obtained as

$$f'_{\text{LyC}} = 1 - \dot{N}_{\text{Ly}\alpha, \text{int}}/0.68/\dot{N}_{\text{LyC}, \text{int}}, \quad (4)$$

where $\dot{N}_{\text{LyC}, \text{int}}$ is the production rate of LyC radiation. Because ground-based observations or local observations do not always have access to Ly α , the H α luminosity is used instead by assuming an intrinsic ratio of $L_{\text{Ly}\alpha}/L_{\text{H}\alpha} \approx 8.7$ after correcting for the attenuation due to dust by using the Balmer decrement ratio ($L_{\text{H}\alpha}/L_{\text{H}\beta} = 2.86$). Together with physical information about individual stars, derived from spectroscopy or photometry, f'_{LyC} can be inferred from HII regions or a section of a galaxy (e.g., Doran et al. 2013; Choi et al. 2020).

Figure 18 examines the validity of these assumptions by comparing the true f_{LyC} with f'_{LyC} deduced from Equation 4. Several important features can be gleaned from the figure. First, although there is significant scatter ($\Delta f_{\text{LyC}} \sim 0.2$), the inferred f'_{LyC} matches f_{LyC} reasonably well down to $f'_{\text{LyC}} \approx 0.1$. Below this, the inference cannot tell whether 30% or none of the photons are escaping. Second, there is a tendency that $f'_{\text{LyC}} < f_{\text{LyC}}$ at $f_{\text{LyC}} \lesssim 0.2$, whereas the opposite is true for $f_{\text{LyC}} \gtrsim 0.4$. The former essentially occurs because collisional radiation becomes important and makes a non-negligible contribution to the total budget of escaping Ly α photons (Smith et al. 2019). Note that during this phase, the typical conditions that generate Ly α photons are $n_{\text{H}} \approx 10^{3.5-4.5} \text{ cm}^{-3}$ and $T \approx 10^{4.1} \text{ K}$. On the other hand, the typical density of Ly α -emitting gas drops to $n_{\text{H}} \sim 5-10 \text{ cm}^{-3}$ in the later phases, and the relative contribution from collision radiation to $L_{\text{Ly}\alpha}$ decreases to $\sim 10\%$. More importantly, in such conditions, recombination occurs slowly and not all of the LyC photons are used to produce Ly α . As a result, Equation 4 tends to over-estimate the true escape fraction. The vertical trend seen near $f'_{\text{esc}} = 1$ in the SM5_pZ014 run

is likely the most dramatic example⁶. The escape fraction is no longer a simple function of the solid angle for optically thick sightlines. Strictly speaking, our Case B assumptions are unlikely to be valid in the optically thin regime, and the use of Case A coefficients would increase the number of Ly α photons by 25% at $T = 10^4$ K. The inferred f'_{LyC} would decrease slightly, but the overall trends should remain the same.

Finally, we remark that the escaping luminosity of the LyC radiation correlates well with the escaping luminosity at 1500 Å (Figure 16, bottom panels). In the case of the SM6_sZ014 run, the escaping luminosities are virtually indistinguishable. This is a coincidence since the escape fractions of 900 Å and 1500 Å photons are significantly different at $t \lesssim 4$ Myr. The similarity arises because the timescale for UV luminosities to reach the maximum from the zero-age main sequence roughly matches the timescale of cloud disruption (~ 3 Myr). The SM6_sZ002 run shows a less tight correlation, but again because the disruption timescale is similar (~ 3 Myr) the escaping luminosity traces f_{LyC} reasonably well. However, GMCs that are dispersed slowly can add complexity to this trend, and the presence of the ISM/CGM can alter the escape fraction of both photons in a different manner. It is thus not conclusive yet if the escaping UV luminosity is a promising proxy to select potential LyC leakers. Cosmological simulations that can resolve individual GMCs are required to assess this possibility.

4.4. Caveats

In this work, we study the propagation of LyC and Ly α from GMCs using high-resolution RMHD simulations, but our work has several limitations and considerable scope for improvement. First, the parameter space we probe is quite limited due to the constraint in computational resources. For example, the only case with low SFE_{tot} ($\sim 1\%$) in our simulations is when strong turbulence is applied, but its physical origin is not justified. An alternative way of simulating GMCs that form stars at a slow rate may be by considering lower gas column densities of $\Sigma \lesssim 50 M_{\odot} \text{pc}^{-2}$ (for $10^5 M_{\odot}$) or $\Sigma \lesssim 100 M_{\odot} \text{pc}^{-2}$ (for $10^6 M_{\odot}$), or by introducing strong magnetic fields (e.g., Kim et al. 2018, 2021b). Furthermore, we do not study the effects of different turbulent seeds on the evolution of GMCs and hence the escape of LyC photons (Grudić et al. 2021b; Kim et al. 2021b), but choose to adopt a different geometry and a high

resolution in this study. Admittedly, even the turbulent structures we employ do not necessarily represent those of high-redshift galaxies that are responsible for reionization. To improve the initial conditions of GMC simulations and to study the propagation of radiation in a realistic setting, high-resolution cosmological galactic-scale simulations are required and are likely possible in the near future.

Second, our simulations lack prescriptions for physical processes that may be dynamically important in GMC environments. Proto-stellar jets and stellar winds are known to provide extra momentum to the surroundings of massive stars, shaping the morphology of HII bubbles (e.g., Rogers & Pittard 2013; Dale et al. 2014; Grudić et al. 2021a; Geen et al. 2021), although winds become relatively less important at lower metallicities. Multiple scattering of Ly α photons (Dijkstra & Loeb 2008; Smith et al. 2017; Kimm et al. 2018; Tomaselli & Ferrara 2021) may accelerate the disruption of dense clumps in the early stage of star formation as well, potentially increasing the escape fractions of LyC photons (Kimm et al. 2019). Inclusion of cosmic rays generated by diffusive shock acceleration can also drive gentle outflows, regulating star formation on a long-term timescale (e.g., Girichidis et al. 2016; Pfrommer et al. 2017; Ruszkowski et al. 2017; Dashyan & Dubois 2020). While understanding the detailed effects of these processes is certainly a challenging task, it is the natural step forward to unravel the complex evolution histories of the GMCs.

Last but not the least, our modeling of dust is likely over-simplified. We assume that 1% of dust survives in an ionized medium (i.e. $f_{\text{dust}}^{\text{ion}} = 0.01$), but observations appear to suggest a wide range of $10^{-4} \lesssim f_{\text{dust}}^{\text{ion}} \lesssim 10^{-1}$ (see Laursen et al. 2009, for the discussion). Although this parameter is not very well constrained, several mechanisms that lower the dust abundance are likely to be at play in HII regions, such as radiation pressure on dust (Draine 2011) or disruption due to radiative torque applied by UV radiation (Hoang et al. 2019), and thus the low $f_{\text{dust}}^{\text{ion}}$ value may be justifiable. In order to gauge the uncertainties associated with $f_{\text{dust}}^{\text{ion}}$, we present the luminosity-weighted Ly α profiles calculated with $f_{\text{dust}}^{\text{ion}} = 0.1$ or 0.001 in Figure 19⁷. We find that the total Ly α escape fraction from the SM6_sZ002 run (54%) is changed to 34% or 58% when $f_{\text{dust}}^{\text{ion}}$ is adjusted to 0.1 or 0.001, respectively. The change in $\langle f_{\text{Ly}\alpha} \rangle$ is more pro-

⁶ The vertical trend seen in the FM6D_sZ002 run occurs because a portion of SN-driven shells are shock-heated, enhancing the recombinative as well as collisional Ly α radiation.

⁷ Note that an increase in the amount of dust hardly affects the escape of LyC radiation as the optical depth to neutral hydrogen is already an order of magnitude larger than that of dust (Kimm et al. 2019), and we focus on the impact on Ly α as the only agent that destroys Ly α is dust, in this study.

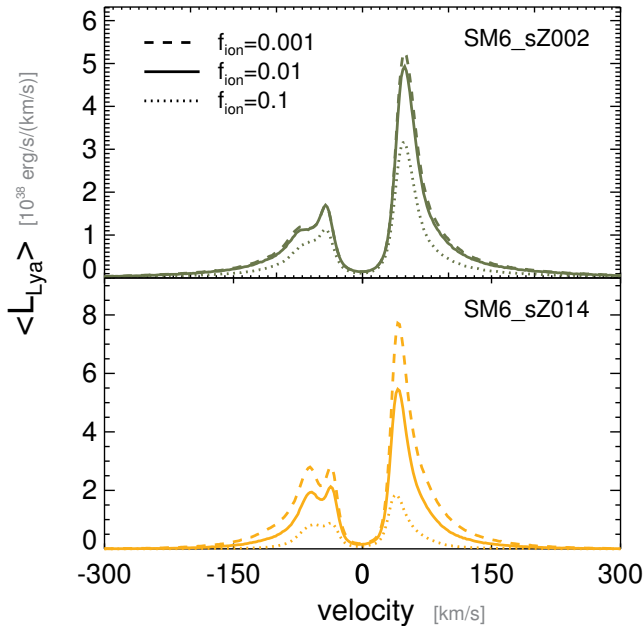


Figure 19. Impact of the choice of $f_{\text{dust}}^{\text{ion}}$, the fraction of dust that survives in ionized media, on the luminosity-weighted Ly α profiles in a metal-poor (SM6_sZ002, top) and metal-rich GMC (SM6_sZ014, bottom). The line profiles are normalized by the bin size of the velocity. Increasing $f_{\text{dust}}^{\text{ion}}$ suppresses the line fluxes, but the velocity separations of the double peaks are barely changed.

nounced in the metal-rich case (SM6_sZ014), with values of 10% ($f_{\text{dust}}^{\text{ion}} = 0.1$) or 45% ($f_{\text{dust}}^{\text{ion}} = 0.001$), compared with 31% in the fiducial case. Nevertheless, the level of uncertainties in the prediction of $f_{\text{Ly}\alpha}$ is unlikely to have a significant impact on our conclusions, and more importantly, the velocity separation is virtually unaffected by the choice of $f_{\text{dust}}^{\text{ion}}$.

5. SUMMARY AND CONCLUSIONS

In this study, we investigated the escape of LyC and Ly α photons from simulated GMCs with diverse physical conditions, with a particular focus on dense and metal-poor clouds, which are likely to be relevant to the evolution of high- z galaxies and reionization. By analyzing 18 high-resolution ($0.02 \leq \Delta x_{\text{min}} \leq 0.08$ pc) RMHD simulations with a self-consistent star formation model based on the sink particle algorithm, we showed that a significant fraction of LyC (≈ 15 –70%) and Ly α photons (≈ 15 –85%) leak from the clouds as they are dispersed rapidly due to stellar feedback. The detailed results can be summarized as follows.

- The escape fractions of LyC and Ly α photons in GMCs generally increase with time as photoionization heating disrupts the clouds very efficiently in $t_{\text{desc}}=3$ –5 Myr. The escaping luminosity of LyC

radiation peaks at ≈ 3 Myr from the onset of star formation (Figure 5), whereas the maximum escaping luminosity of Ly α photons tends to occur earlier at 1–2 Myr (Figure 6). These timescales are larger in a homogeneous cloud where the gas surface density is lower.

- The time-integrated escape fraction of ionizing radiation ($\langle f_{\text{LyC}} \rangle$) reveals a strong correlation with the total SFE, showing a maximum at $\text{SFE}_{\text{tot}} \approx 20\%$ (Figure 14). LyC leakage is less notable in GMCs with lower SFE_{tot} because of the finite number of LyC photons, while the propagation is suppressed in GMCs with high SFE_{tot} because their extreme gas densities prevent the rapid development of ionized bubbles (Figure 15).
- Consistent with previous findings, less massive clouds with $10^5 M_{\odot}$ show a larger LyC escape fraction of $\sim 60\%$, while a more massive cloud with $10^6 M_{\odot}$ reveals a lower $\langle f_{\text{LyC}} \rangle$ of $\sim 40\%$. The difference is partly driven by the higher gas surface density adopted in the more massive GMCs. Indeed, the smallest fraction ($\approx 15\%$) of LyC radiation escapes from the high-mass GMC with an extremely high Σ_{gas} of $1000 M_{\odot} \text{pc}^{-2}$.
- Metal-rich clouds tend to show lower $\langle f_{\text{LyC}} \rangle$ and $\langle f_{\text{Ly}\alpha} \rangle$ than metal-poor GMCs by 15–31% and 22–45%, respectively, although their SFE_{tot} are sometimes higher. We attribute this to additional cooling due to metals, which weakens the effect of photoionization heating.
- The escape of LyC and Ly α photons is suppressed in a GMC with strong turbulence as SFE_{tot} is dramatically reduced and the number of LyC photons become finite. On the other hand, only marginal differences in $\langle f_{\text{LyC}} \rangle$ and $\langle f_{\text{Ly}\alpha} \rangle$ are found between clouds with different morphologies (spherical versus filamentary), magnetic field strengths, and the presence of SNe, although filamentary structures allow for more efficient Ly α escape.
- Ly α photons escape most efficiently from their birth clouds in the middle of cloud disruption (Figure 8). The velocity separation of the double peak in the Ly α spectrum is initially very large ($v_{\text{sep}} \sim 500 \text{ km s}^{-1}$), but the luminosity-weighted spectrum reveals a smaller v_{sep} of $\approx 120 \text{ km s}^{-1}$ (Figure 10). The velocity separation as well as the evolutionary locus in the $v_{\text{sep}}-f_{900}$ plane turn out to be similar, regardless of the properties of the simulated GMCs (Figure 10 and 12), suggesting

that these measurements may reveal more about the properties of the ISM and CGM of galaxies rather than their molecular clouds.

- The escape fraction of Ly α photons is systematically larger than that of LyC ($f_{\text{Ly}\alpha} \approx f_{900}^{0.27}$) (Figure 12). Despite the significant difference in the absorption probability owing to dust, the correlation with the escape of UV photons at 1500Å is found to be equally strong as that of Ly α as clumpy gas distributions lead to an absorption of both Ly α and the UV photons, while some photons escape through low column density channels (Figure 17). By contrast, the correlation between f_{900} and $f_{\text{H}\alpha}$ is found to be very weak, as $f_{\text{H}\alpha}$ is usually very high.
- f_{LyC} may be best inferred from Ly α luminosities by assuming recombination in the optically thick regime (Equation 4 and Figure 18). Although there is a significant scatter ($\Delta f \sim 0.2$), the inferred escape fraction shows a reasonable one-to-one correspondence at $f_{\text{LyC}} \gtrsim 0.1$. However, there is a fair chance that the approach may underestimate the true f_{LyC} at low $f_{\text{LyC}} \lesssim 0.2$ due to the neglect of collisional radiation, or may overestimate at high $f_{\text{LyC}} \gtrsim 0.4$ because the optically thick assumption is no longer valid.

We remark that the escape of ionizing radiation from our gravitationally well-bound GMCs is overall more efficient than required to fully ionize the Universe by $z = 6$ (e.g., Robertson et al. 2015; Rosdahl et al. 2018, $\langle f_{\text{LyC}} \rangle \sim 10\%$). However, this is not a concern because the absorption of LyC by the ISM is significant. As shown by Yoo et al. (2020), the escape fraction in disk galaxies can easily drop from $\sim 50\%$ at the 100 pc scale to $\sim 10\%$ by the time LyC photons leave their host dark matter halo. Moreover, observations of local GMCs or star forming regions often reveal extremely large f_{LyC}

(Pellegrini et al. 2012; Doran et al. 2013; McLeod et al. 2019; Choi et al. 2020; Della Bruna et al. 2021). The question remains though, whether the properties of the local GMCs can be applicable to those in high- z galaxies. Combined efforts based on upcoming observing facilities and state-of-the-art simulations are required to further shed light on the role of LyC photons from GMCs in the evolution of galaxies and reionization, and to exploit the useful information in galactic Ly α spectra.

ACKNOWLEDGEMENTS

TK was supported by the National Research Foundation of Korea (NRF-2019K2A9A1A06091377 and 2020R1C1C1007079). SG acknowledges support from a NOVA grant for the theory of massive star formation. This work was supported by the Programme National Cosmologie et Galaxies (PNCG) of CNRS/INSU with INP and IN2P3, co-funded by CEA and CNES. We additionally acknowledge support and computational resources from the Common Computing Facility (CCF) of the LABEX Lyon Institute of Origins (ANR-10-LABX-66). The supercomputing time for numerical simulations was kindly provided by KISTI (KSC-2019-CRE-0196), and large data transfer was supported by KREONET, which is managed and operated by KISTI. This work also used the DiRAC Complexity system, operated by the University of Leicester IT Services, which forms part of the STFC DiRAC HPC Facility (www.dirac.ac.uk). Some of the simulations in this paper were performed on the Dutch National Supercomputing cluster Cartesius at SURFsara and on the draco cluster hosted by the Max Planck Computing and Data Facility (<http://www.mpcdf.mpg.de/>). The authors gratefully acknowledge the data storage service SDS@hd supported by the Ministry of Science, Research and the Arts Baden-Württemberg (MWK) and the German Research Foundation (DFG) through grant INST35/1314-1FUGG.

APPENDIX

A. EFFECTS OF RESOLUTION

The evolution of GMCs is often affected by the numerical resolution because the Stromgren radius and the cooling length of SN driven shells become progressively small with increasing density. Therefore, we investigate whether our results numerically converge by comparing SFE_{tot} and escape fractions.

The left panels in Figure 20 show that f_{LyC} and $f_{\text{Ly}\alpha}$ in the small cloud of mass $10^5 M_{\odot}$ are almost indistinguishable at minimum cell widths in the range 0.02–0.08 pc. On the other hand, differences in SFE_{tot} in different resolution runs are more perceptible. Our fiducial case with a minimum 0.04 pc resolution converts 25.7% of gas into stars, but the fraction decreases to 19.2% in a lower-resolution simulation (SM5_pZ002_LR). However, there is no systematic trend of an increase in the resolution leading to a higher SFE_{tot} , as our highest resolution run produces 23.9% of stars. This

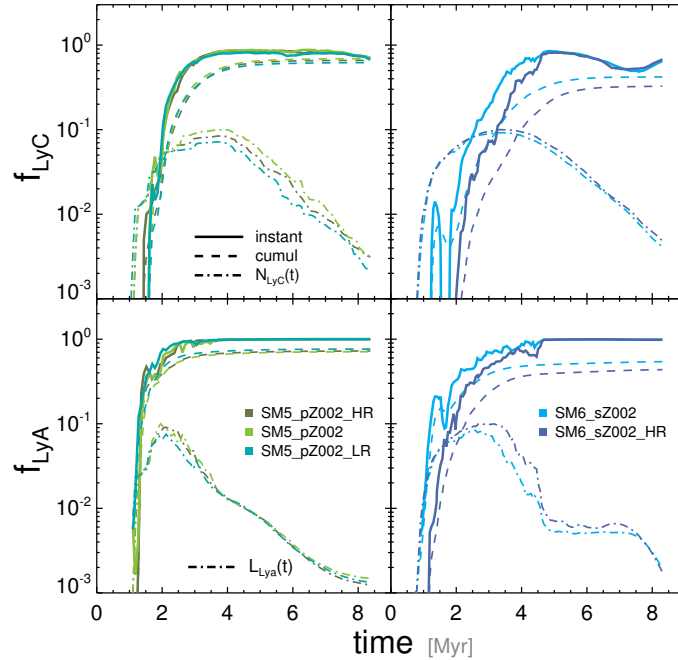


Figure 20. Effect of resolutions on the escape of LyC and Ly α radiation. The results from the runs with varying resolutions are shown as different color-codings. The solid and dashed lines show instantaneous and cumulative escape fractions, respectively, while the dot-dashed lines correspond to the number of LyC photons or intrinsic Ly α luminosity, as indicated in the legend.

indicates that our simulation results are likely to converge reasonably at resolutions in the range 0.02–0.04 pc, but the results for a resolution of 0.08 pc may still be acceptable within an accuracy of about 20%.

The right panels in Figure 20 further shows the effects of the resolution in a more massive cloud with $10^6 M_{\odot}$. Unlike small GMCs, the differences in f_{LyC} and $f_{\text{Ly}\alpha}$ are larger, despite the differences in SFE_{tot} between the fiducial (SM6_sZ002, 0.510) and higher-resolution run (SM6_sZ002_HR, 0.549) being small. The $\langle f_{\text{LyC}} \rangle$ value in the 0.08 pc resolution run is 54.2%, but this is reduced to 43.6%, which again differ by $\approx 20\%$. This may not be negligible, but we argue that a relative comparison between runs with the same resolution should still be useful as it allows us to study the physical origin of the potential differences in f_{LyC} and $f_{\text{Ly}\alpha}$ between different settings.

REFERENCES

- Ahn, S.-H., Lee, H.-W., & Lee, H. M. 2003, MNRAS, 340, 863
- Atek, H., Richard, J., Kneib, J.-P., & Schaerer, D. 2018, MNRAS, 479, 5184
- Audit, E., & Hennebelle, P. 2005, A&A, 433, 1
- Barnes, L. A., Haehnelt, M. G., Tescari, E., & Viel, M. 2011, MNRAS, 416, 1723
- Bennett, J. S., & Sijacki, D. 2020, MNRAS, 499, 597
- Bleuler, A., & Teyssier, R. 2014, MNRAS, 445, 4015
- Borisova, E., Cantalupo, S., Lilly, S. J., et al. 2016, ApJ, 831, 39
- Byrohl, C., Nelson, D., Behrens, C., et al. 2021, MNRAS, 506, 5129
- Cantalupo, S., Arrigoni-Battaia, F., Prochaska, J. X., Hennawi, J. F., & Madau, P. 2014, Nature, 506, 63
- Chabrier, G. 2003, PASP, 115, 763
- Charlot, S., & Fall, S. M. 1993, ApJ, 415, 580
- Chevance, M., Kruijssen, J. M. D., Hygate, A. P. S., et al. 2020, MNRAS, 493, 2872
- Choi, Y., Dalcanton, J. J., Williams, B. F., et al. 2020, ApJ, 902, 54
- Colombo, D., Hughes, A., Schinnerer, E., et al. 2014, ApJ, 784, 3
- Dale, J. E., Ercolano, B., & Bonnell, I. A. 2012, MNRAS, 424, 377
- . 2013, MNRAS, 430, 234
- Dale, J. E., Ngoumou, J., Ercolano, B., & Bonnell, I. A. 2014, MNRAS, 442, 694
- Dashyan, G., & Dubois, Y. 2020, A&A, 638, A123
- Dayal, P., & Ferrara, A. 2018, PhR, 780, 1
- Della Bruna, L., Adamo, A., Lee, J. C., et al. 2021, A&A, 650, A103

- Dijkstra, M. 2014, *PASA*, 31, e040
- Dijkstra, M., Gronke, M., & Venkatesan, A. 2016, *ApJ*, 828, 71
- Dijkstra, M., Haiman, Z., & Spaans, M. 2006, *ApJ*, 649, 14
- Dijkstra, M., & Loeb, A. 2008, *MNRAS*, 391, 457
- Doran, E. I., Crowther, P. A., de Koter, A., et al. 2013, *A&A*, 558, A134
- Doussot, A., Trac, H., & Cen, R. 2019, *ApJ*, 870, 18
- Draine, B. T. 2011, *ApJ*, 732, 100
- Ekström, S., Georgy, C., Eggenberger, P., et al. 2012, *A&A*, 537, A146
- Erb, D. K., Steidel, C. C., Trainor, R. F., et al. 2014, *ApJ*, 795, 33
- Finlator, K., Keating, L., Oppenheimer, B. D., Davé, R., & Zackrisson, E. 2018, *ArXiv e-prints*
- Fromang, S., Hennebelle, P., & Teyssier, R. 2006, *A&A*, 457, 371
- Fukushima, H., Yajima, H., Sugimura, K., et al. 2020, *MNRAS*, 497, 3830
- Garel, T., Blaizot, J., Rosdahl, J., et al. 2021, *MNRAS*
- Gazagnes, S., Chisholm, J., Schaerer, D., Verhamme, A., & Izotov, Y. 2020, *A&A*, 639, A85
- Gazagnes, S., Chisholm, J., Schaerer, D., et al. 2018, *A&A*, 616, A29
- Geen, S., Bieri, R., Rosdahl, J., & de Koter, A. 2021, *MNRAS*, 501, 1352
- Geen, S., Soler, J. D., & Hennebelle, P. 2017, *MNRAS*, 471, 4844
- Geen, S., Watson, S. K., Rosdahl, J., et al. 2018, *MNRAS*, 481, 2548
- Georgy, C., Ekström, S., Eggenberger, P., et al. 2013, *A&A*, 558, A103
- Girichidis, P., Seifried, D., Naab, T., et al. 2018, *MNRAS*, 480, 3511
- Girichidis, P., Naab, T., Walch, S., et al. 2016, *ApJL*, 816, L19
- Gnedin, N. Y. 2014, *ApJ*, 793, 29
- Górski, K. M., Hivon, E., Banday, A. J., et al. 2005, *ApJ*, 622, 759
- Götberg, Y., de Mink, S. E., McQuinn, M., et al. 2020, *A&A*, 634, A134
- Gronke, M. 2017, *A&A*, 608, A139
- Gronke, M., Girichidis, P., Naab, T., & Walch, S. 2018, *ApJL*, 862, L7
- Gronke, M., & Oh, S. P. 2018, *MNRAS*, 480, L111
- Grudić, M. Y., Guszejnov, D., Hopkins, P. F., Offner, S. S. R., & Faucher-Giguère, C.-A. 2021a, *MNRAS*, 506, 2199
- Grudić, M. Y., Kruijssen, J. M. D., Faucher-Giguère, C.-A., et al. 2021b, *MNRAS*, 506, 3239
- Guillet, T., & Teyssier, R. 2011, *Journal of Computational Physics*, 230, 4756
- Hansen, M., & Oh, S. P. 2006, *MNRAS*, 367, 979
- He, C.-C., Ricotti, M., & Geen, S. 2020, *MNRAS*, 492, 4858
- Hennebelle, P., & Iffrig, O. 2014, *A&A*, 570, A81
- Heyer, M., Krawczyk, C., Duval, J., & Jackson, J. M. 2009, *ApJ*, 699, 1092
- Hoang, T., Tram, L. N., Lee, H., & Ahn, S.-H. 2019, *Nature Astronomy*, 3, 766
- Howard, C. S., Pudritz, R. E., Harris, W. E., & Klessen, R. S. 2018, *MNRAS*, 475, 3121
- Hui, L., & Gnedin, N. Y. 1997, *MNRAS*, 292, 27
- Hummels, C. B., Smith, B. D., Hopkins, P. F., et al. 2019, *ApJ*, 882, 156
- Hutter, A., Dayal, P., Yepes, G., et al. 2021, *MNRAS*, 503, 3698
- Iben, Icko, J. 1967, *ARA&A*, 5, 571
- Iliev, I. T., Mellema, G., Pen, U. L., et al. 2006, *MNRAS*, 369, 1625
- Izotov, Y. I., Orlová, I., Schaerer, D., et al. 2016a, *Nature*, 529, 178
- Izotov, Y. I., Schaerer, D., Thuan, T. X., et al. 2016b, *MNRAS*, 461, 3683
- Izotov, Y. I., Schaerer, D., Worseck, G., et al. 2018, *MNRAS*, 474, 4514
- Izotov, Y. I., Worseck, G., Schaerer, D., et al. 2021, *MNRAS*, 503, 1734
- Jung, I., Finkelstein, S. L., Dickinson, M., et al. 2020, *ApJ*, 904, 144
- Kakiichi, K., & Gronke, M. 2021, *ApJ*, 908, 30
- Katz, H., Ďurovčíková, D., Kimm, T., et al. 2020, *MNRAS*, 498, 164
- Kim, C.-G., & Ostriker, E. C. 2015, *ApJ*, 802, 99
- Kim, J., Chevance, M., Kruijssen, J. M. D., et al. 2021a, *MNRAS*, 504, 487
- Kim, J.-G., Kim, W.-T., & Ostriker, E. C. 2018, *ApJ*, 859, 68
- . 2019, *ApJ*, 883, 102
- Kim, J.-G., Ostriker, E. C., & Filippova, N. 2021b, *ApJ*, 911, 128
- Kimm, T., Blaizot, J., Garel, T., et al. 2019, *MNRAS*, 486, 2215
- Kimm, T., & Cen, R. 2014, *ApJ*, 788, 121
- Kimm, T., Haehnelt, M., Blaizot, J., et al. 2018, *MNRAS*, 475, 4617
- Kimm, T., Katz, H., Haehnelt, M., et al. 2017, *MNRAS*, 466, 4826
- Krumholz, M. R., Stone, J. M., & Gardiner, T. A. 2007, *ApJ*, 671, 518

- Laursen, P., Sommer-Larsen, J., & Andersen, A. C. 2009, *ApJ*, 704, 1640
- Leclercq, F., Bacon, R., Wisotzki, L., et al. 2017, *A&A*, 608, A8
- Liu, L., Bureau, M., Blitz, L., et al. 2021, *MNRAS*, 505, 4048
- Livermore, R. C., Finkelstein, S. L., & Lotz, J. M. 2017, *ApJ*, 835, 113
- Lopez, L. A., Krumholz, M. R., Bolatto, A. D., et al. 2014, *ApJ*, 795, 121
- Madau, P., Haardt, F., & Rees, M. J. 1999, *ApJ*, 514, 648
- Malhotra, S., & Rhoads, J. E. 2002, *ApJL*, 565, L71
- Matzner, C. D. 2002, *ApJ*, 566, 302
- Mauerhofer, V., Verhamme, A., Blaizot, J., et al. 2021, *A&A*, 646, A80
- McCourt, M., Oh, S. P., O’Leary, R., & Madigan, A.-M. 2018, *MNRAS*, 473, 5407
- McLeod, A. F., Dale, J. E., Evans, C. J., et al. 2019, *MNRAS*, 486, 5263
- McLeod, A. F., Kruijssen, J. M. D., Weisz, D. R., et al. 2020, *ApJ*, 891, 25
- Mesinger, A., & Furlanetto, S. 2007, *ApJ*, 669, 663
- Michel-Dansac, L., Blaizot, J., Garel, T., et al. 2020, *A&A*, 635, A154
- Mitchell, P. D., Blaizot, J., Cadiou, C., et al. 2021, *MNRAS*, 501, 5757
- Neufeld, D. A. 1990, *ApJ*, 350, 216
- Norman, M. L., Reynolds, D. R., So, G. C., Harkness, R. P., & Wise, J. H. 2015, *ApJS*, 216, 16
- Ocvirk, P., Gillet, N., Shapiro, P. R., et al. 2016, *MNRAS*, 463, 1462
- Orlitová, I., Verhamme, A., Henry, A., et al. 2018, *A&A*, 616, A60
- O’Shea, B. W., Wise, J. H., Xu, H., & Norman, M. L. 2015, *ApJL*, 807, L12
- Osterbrock, D. E., & Ferland, G. J. 2006, *Astrophysics of gaseous nebulae and active galactic nuclei*
- Ouchi, M., Ono, Y., & Shibuya, T. 2020, *ARA&A*, 58, 617
- Partridge, R. B., & Peebles, P. J. E. 1967, *ApJ*, 147, 868
- Pawlik, A. H., Rahmati, A., Schaye, J., Jeon, M., & Dalla Vecchia, C. 2017, *MNRAS*, 466, 960
- Pellegrini, E. W., Oey, M. S., Winkler, P. F., et al. 2012, *ApJ*, 755, 40
- Pentericci, L., Fontana, A., Vanzella, E., et al. 2011, *ApJ*, 743, 132
- Pfrommer, C., Pakmor, R., Schaal, K., Simpson, C. M., & Springel, V. 2017, *MNRAS*, 465, 4500
- Robertson, B. E., Ellis, R. S., Furlanetto, S. R., & Dunlop, J. S. 2015, *ApJL*, 802, L19
- Rogers, H., & Pittard, J. M. 2013, *MNRAS*, 431, 1337
- Roman-Duval, J., Jackson, J. M., Heyer, M., Rathborne, J., & Simon, R. 2010, *ApJ*, 723, 492
- Rosdahl, J., Blaizot, J., Aubert, D., Stranex, T., & Teyssier, R. 2013, *MNRAS*, 436, 2188
- Rosdahl, J., & Teyssier, R. 2015, *MNRAS*, 449, 4380
- Rosdahl, J., Katz, H., Blaizot, J., et al. 2018, *MNRAS*, 479, 994
- Ruszkowski, M., Yang, H. Y. K., & Zweibel, E. 2017, *ApJ*, 834, 208
- Safarzadeh, M., & Scannapieco, E. 2016, *ApJL*, 832, L9
- Santos, S., Sobral, D., Matthee, J., et al. 2020, *MNRAS*, 493, 141
- Secunda, A., Cen, R., Kimm, T., Götberg, Y., & de Mink, S. E. 2020, *ApJ*, 901, 72
- Semenov, V. A., Kravtsov, A. V., & Gnedin, N. Y. 2021, *arXiv e-prints*, arXiv:2103.13406
- Smith, A., Bromm, V., & Loeb, A. 2017, *MNRAS*, 464, 2963
- Smith, A., Ma, X., Bromm, V., et al. 2019, *MNRAS*, 484, 39
- Smith, A., Safranek-Shrader, C., Bromm, V., & Milosavljević, M. 2015, *MNRAS*, 449, 4336
- Song, H., Seon, K.-I., & Hwang, H. S. 2020, *ApJ*, 901, 41
- Sparre, M., Pfrommer, C., & Vogelsberger, M. 2019, *MNRAS*, 482, 5401
- Stanway, E. R., Eldridge, J. J., & Becker, G. D. 2016, *MNRAS*, 456, 485
- Stark, D. P., Ellis, R. S., & Ouchi, M. 2011, *ApJL*, 728, L2
- Storey, P. J., & Hummer, D. G. 1995, *MNRAS*, 272, 41
- Sutherland, R. S., & Dopita, M. A. 1993, *ApJS*, 88, 253
- Teyssier, R. 2002, *A&A*, 385, 337
- Tomaselli, G. M., & Ferrara, A. 2021, *MNRAS*, 504, 89
- Topping, M. W., & Shull, J. M. 2015, *ApJ*, 800, 97
- Trebitsch, M., Blaizot, J., Rosdahl, J., Devriendt, J., & Slyz, A. 2017, *MNRAS*, 470, 224
- van de Voort, F., Springel, V., Mandelker, N., van den Bosch, F. C., & Pakmor, R. 2019, *MNRAS*, 482, L85
- Vanzella, E., de Barros, S., Castellano, M., et al. 2015, *A&A*, 576, A116
- Vanzella, E., Nonino, M., Cupani, G., et al. 2018, *MNRAS*, 476, L15
- Vanzella, E., Meneghetti, M., Caminha, G. B., et al. 2020, *MNRAS*, 494, L81
- Verhamme, A., Dubois, Y., Blaizot, J., et al. 2012, *A&A*, 546, A111
- Verhamme, A., Orlitová, I., Schaerer, D., & Hayes, M. 2015, *A&A*, 578, A7
- Verhamme, A., Orlitová, I., Schaerer, D., et al. 2017, *A&A*, 597, A13

- Verhamme, A., Schaerer, D., & Maselli, A. 2006, *A&A*, 460, 397
- Weingartner, J. C., & Draine, B. T. 2001, *ApJ*, 548, 296
- Wise, J. H., Demchenko, V. G., Halicek, M. T., et al. 2014, *MNRAS*, 442, 2560
- Wisotzki, L., Bacon, R., Blaizot, J., et al. 2016, *A&A*, 587, A98
- Wong, T., Hughes, A., Ott, J., et al. 2011, *ApJS*, 197, 16
- Xu, H., Wise, J. H., Norman, M. L., Ahn, K., & O'Shea, B. W. 2016, *ApJ*, 833, 84
- Yajima, H., Li, Y., Zhu, Q., et al. 2014, *MNRAS*, 440, 776
- Yan, M., Sadeghpour, H. R., & Dalgarno, A. 2001, *ApJ*, 559, 1194
- Yang, H., Malhotra, S., Gronke, M., et al. 2016, *ApJ*, 820, 130
- Yoo, T., Kimm, T., & Rosdahl, J. 2020, *MNRAS*, 499, 5175
- Zheng, Z., & Miralda-Escudé, J. 2002, *ApJ*, 578, 33